Check for updates

PALEONTOLOGY

The rise of lichens during the colonization of terrestrial environments

Bruno Becker-Kerber^{1,2,3}*, Jochen J. Brocks⁴, Nathaly L. Archilha¹, Cristiane B. Rodella¹, Valeri Petkov⁵, Eduardo R. deAzevedo⁶, Tairine Pimentel⁷, Rodrigo Garcia⁶, Duane Petts⁸, Janina Czas⁸, Omid H. Ardakani⁹, Anthony Chappaz⁵, Ângela Albuquerque¹⁰, Javier Ortega-Hernández³, Rudy Lerosey-Aubril³, Michael A. Kipp¹¹, Benjamin Johnson¹², Mathieu Thoury¹³, Cecilia M. A. Oliveira¹⁴, Hannah H. L. S. M. Pimentel¹⁴, Raul O. Freitas¹, Flavio C. Vicentin¹, Luiz G. F. Borges¹, Jonathan Almer¹⁵, Jun-Sang Park¹⁵, Carla C. Polo^{1,16}, Gilmar Kerber¹⁷, Lucas del Mouro³, Milene Figueiredo¹⁸, Gustavo M. E. M. Prado², Sharif Ahmed¹⁹, Miguel A. S. Basei²

The origin of terrestrial life and ecosystems fundamentally changed the biosphere. Lichens, symbiotic fungi-algae partnerships, are crucial to nutrient cycling and carbon fixation today, yet their evolutionary history during the evolution of terrestrial ecosystems remains unclear due to a scarce fossil record. We demonstrate that the enigmatic Devonian fossil *Spongiophyton* from Brazil captures one of the earliest and most widespread records of lichens. The presence of internal hyphae networks, algal cells, possible reproductive structures, calcium oxalate pseudomorphs, abundant nitrogenous compounds, and fossil lipid composition confirms that it was among the first widespread representatives of lichenized fungi in Earth's history. *Spongiophyton* abundance and wide paleogeographic distribution in Devonian successions reveal an ecologically prominent presence of lichens during the late stages of terrestrial colonization, just before the evolution of complex forest ecosystems.

Copyright @ 2025 the authors; exclusive licensee American Association for the Advancement of Science subject to Canadian Crown copyright, © His Majesty the King in Right of Canada, as represented by the Minister of the Environment, 2025. Distributed under a Creative Commons Attribution NonCommercial License 4.0 (CC BY-NC).

INTRODUCTION

The colonization of land and the subsequent evolution of complex land ecosystems was one of the most marked evolutionary events in the history of life. This process has markedly affected both land and marine settings, contributing to drawdown of atmospheric CO₂, increased weathering and nutrient input to oceans, soil development, and the evolution of major groups of terrestrial animals (1). Early plants are well-known to have been central to the colonization of land, particularly producing the first cryptogamic ecosystems (2). The earliest evidence of basal embryophytes occurs as cryptospores by the Middle Ordovician (3, 4), while macrofossils of early vascular plants appear in Silurian deposits (5). However, the role and presence of lichens during certain steps of the terrestrialization process remain unclear (6), although this group is a major component of modern cryptogamic covers.

According to some molecular clock estimates, modern lichen lineages did not evolve before vascular plants, based largely on calibrations using well-preserved Cenozoic amber fossils (6). Although crown-group embryophytes and crown-tracheophytes likely preceded the emergence of lichenized fungi, the rarity and ambiguous

¹Brazilian Synchrotron Light Laboratory, Campinas, Brazil. ²Universidade de São Paulo, São Paulo, Brazil. ³Harvard University, Cambridge, MA, USA. ⁴Australian National University, Canberra, Australia. ⁵Central Michigan University, Mount Pleasant, MI, USA. ⁶Universidade de São Paulo, São Carlos, SP, Brazil. ⁷Universidade Estadual do Oeste do Paraná, Toledo, PR, Brazil. ⁸Geological Survey of Canada, Ottawa, Canada. ⁹Natural Resources Canada, Calgary, Canada. ¹⁰Brazilian Nanotechnology National Laboratory, Campinas, Brazil. ¹¹Duke University, Durham, NC, USA. ¹²Iowa State University, Ames, IA, USA. ¹³Institut photonique d'analyse non-destructive européen des matériaux anciens, Saint-Aubin, France. ¹⁴Universidade Federal de Goiás, Goiás, Brazil. ¹⁵Argonne National Laboratory, Lemont, IL, USA. ¹⁶Universidade Estadual de Campinas, Campinas, SP, Brazil. ¹⁷Universidade Federal de Mato Grosso do Sul, Campo Grande, Brazil. ¹⁸PETROBRAS, Rio de Janeiro, Brazil. ¹⁹Diamond Light Source, Didcot, UK.

*Corresponding author. Email: bkerber@fas.harvard.edu

preservation of early lichen-like fossils provide little insight into this critical step in the evolution of terrestrial biota (7, 8). The fossil record of lichens is notably poor, despite their ecological importance in modern terrestrial environments. Older occurrences are scarce and challenging to interpret, largely due to not only lack of preserved diagnostic features but also their gross morphology being similar to many different modern groups of organisms (7).

Among the Paleozoic candidates, Spongiophyton stands out as an abundant and widespread genus with long-lasting enigmatic affinities. It was suggested to have a lichen nature by some authors (9-11), but it is mostly regarded as an alga or early nonvascular plant (12-14). Recent chemical investigations of Spongiophyton suggested similarities with both bryophytes and lichens (15), although most infrared absorption bands reported reflect mineral contamination (see the Supplementary Materials). Spongiophyton is a millimeter wide fossil with dichotomously branching and dorsiventrally organized thalli composed of a poral and aporal surface. These fossils are usually preserved as thick carbonaceous compressions, often called "cuticles." Here, we studied abundant and well-preserved carbonaceous remains of Spongiophyton from Early Devonian [~410 million years (Ma)] rocks of Brazil. We use multiple advanced synchrotron radiation (SR) and laboratory-based methods to thoroughly investigate the morphology, chemistry, and mineralogy of Spongiophyton.

RESULTS AND DISCUSSION

Morphology

The studied material consists of specimens of *Spongiophyton nanum* (Figs. 1 to 3) from the Pragian-Emsian Ponta Grossa Formation in the Paraná Basin of Brazil. The fossils were found as a connected mass of abundant thalli showing a broadly semiradial distribution of its elements (Fig. 2A). The thalli are 2.7 mm wide and a few centimeters long and bear pores of $214 \, \mu m$ in maximum width (133 to

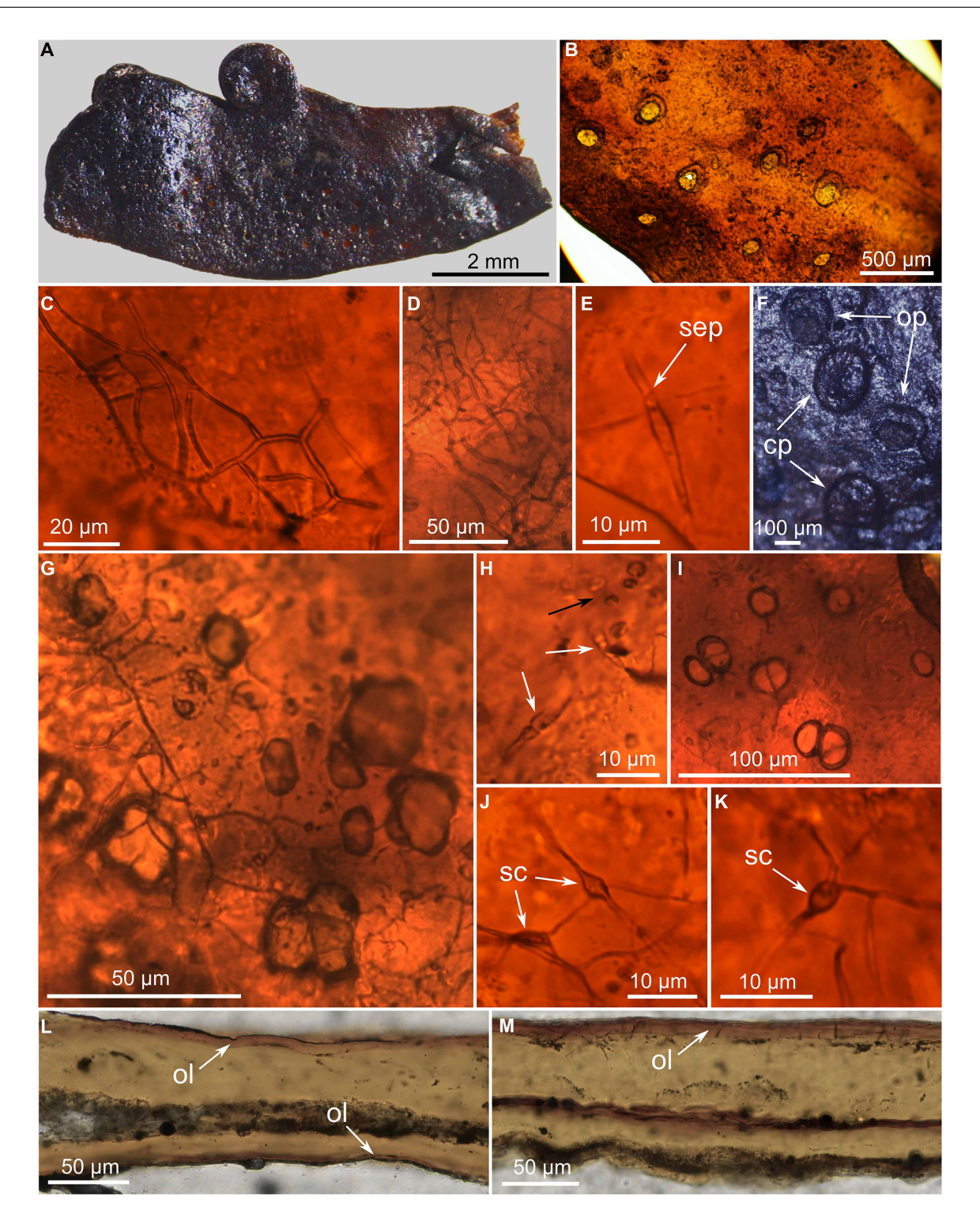


Fig. 1. Morphology and internal structures of *S. nanum*. (A) Isolated fragment of the thalli showing upper surface with pores. (B) Fragment under transmitted light. (C and D) Anastomosing hyphae. (E) Hypha with septum (sep). (F) Stereomicroscope image of the upper surface with open (op) and closed pores (cp). (G) Hyphae associated with and branching toward photobiont cells and cell packages. (H) Putative asci- or conidium-like structures (white arrows) and possible spores (black arrow). (I) Cells and cell packages. (J and K) Swollen cells (sc). (L and M) Thin sections with longitudinal cuts illustrating the outermost upper layer (ol) on the upper surface.

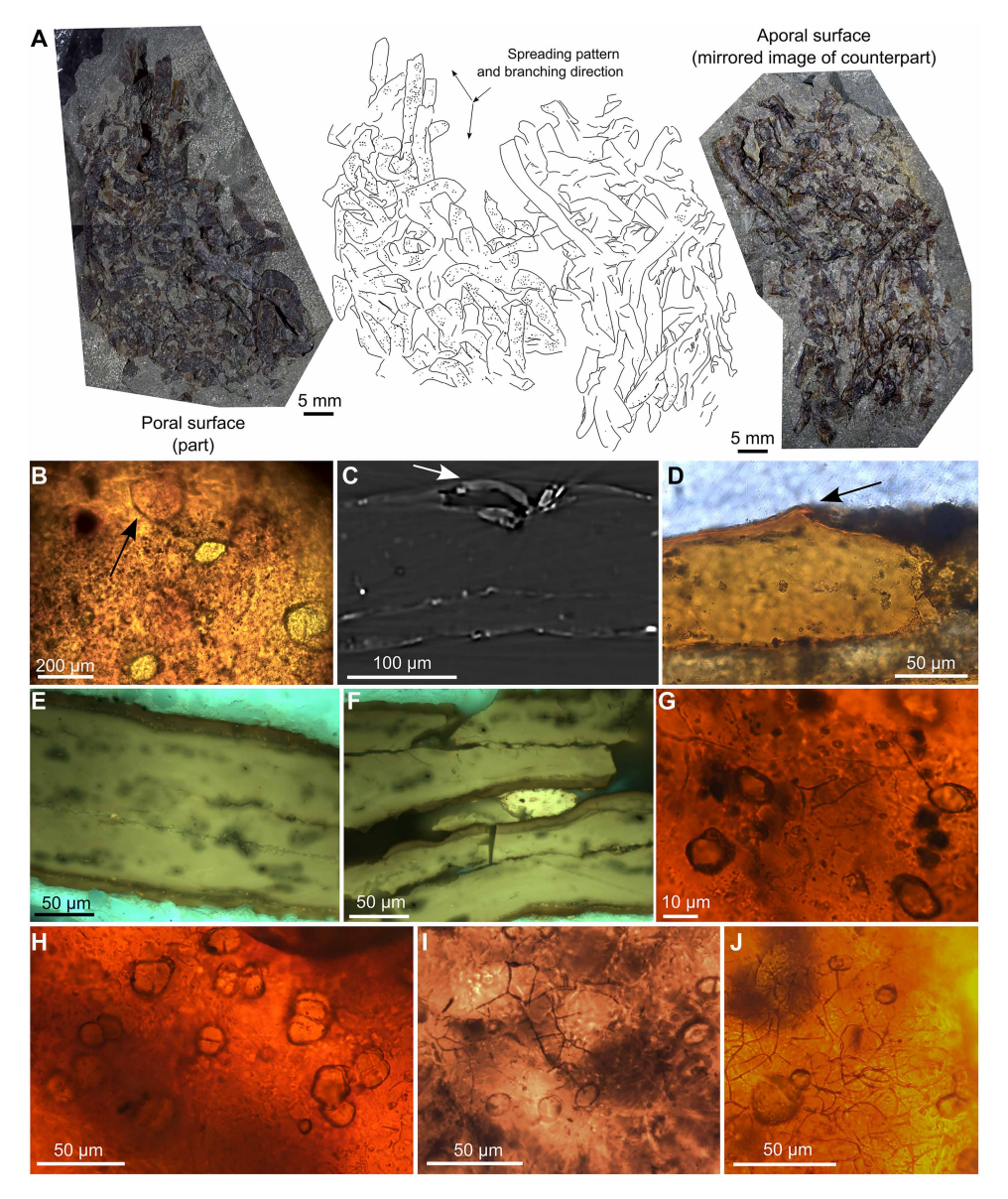


Fig. 2. Thalli disposition and internal cellular structures. (A) Slab with *S. nanum* connected thalli elements showing their distribution on the bedding plane. (B) Optical microscope image showing open and closed pores (arrow). (C) Slice from SR-nanoCT in the region of an open pore showing remnants of the former cover. (D) Poral covering remnants observed by transmitted light. (E and F) Bright yellow algae and dark yellowish green thalli under reflected fluorescence light. (G to J) Photobiont cells and cell packages strongly associated with hyphae networks.

303 µm; data S1). In a few cases, the pores appear covered by a domed layer or cap-like structure (Figs. 1F and 2B).

Fine (\leq 6 μ m) outermost layers are observed in thin sections (Fig. 1, L and M), with no discernible cellular structure. The outer layers of the poral surface are usually thicker and more commonly preserved than the outer layers of the aporal surface (Figs. 1, L and M; and 2, E and F). Most thalli elements show internal networks of hyphae (Figs. 1, C to E, 2, G to J, and 3, D to F; and fig. S1) that are 2.12 μ m in mean diameter (n=157). Most hyphae run roughly parallel to each other and to the surface of the thalli, although different orientations are present (fig. S1A). Septa (Fig. 1E and fig. S1F), swollen cells (Fig. 1, J and K), and putative

reproductive structures associated with spore-like features are also present (Fig. 1H).

The hyphae often occur closely associated with large spherical cells or cell clusters (5 to 37 µm) (Figs. 1, G and I, 2, G to J, and 3). In optical microscopy, these cells occur close to the poral surface outer layers or even at the surface of the thalli if this outer layer is not preserved. Similarly sized but apparently compressed cellular packages are visible just below the poral surface in SR nanotomography (SR-nanoCT) images (Fig. 3, B to D).

Although the remains of *S. nanum* were transported to an offshore marine setting (see the Supplementary Materials), all the thalli elements exhibit a consistent orientation of the poral surface (Fig. 2A).

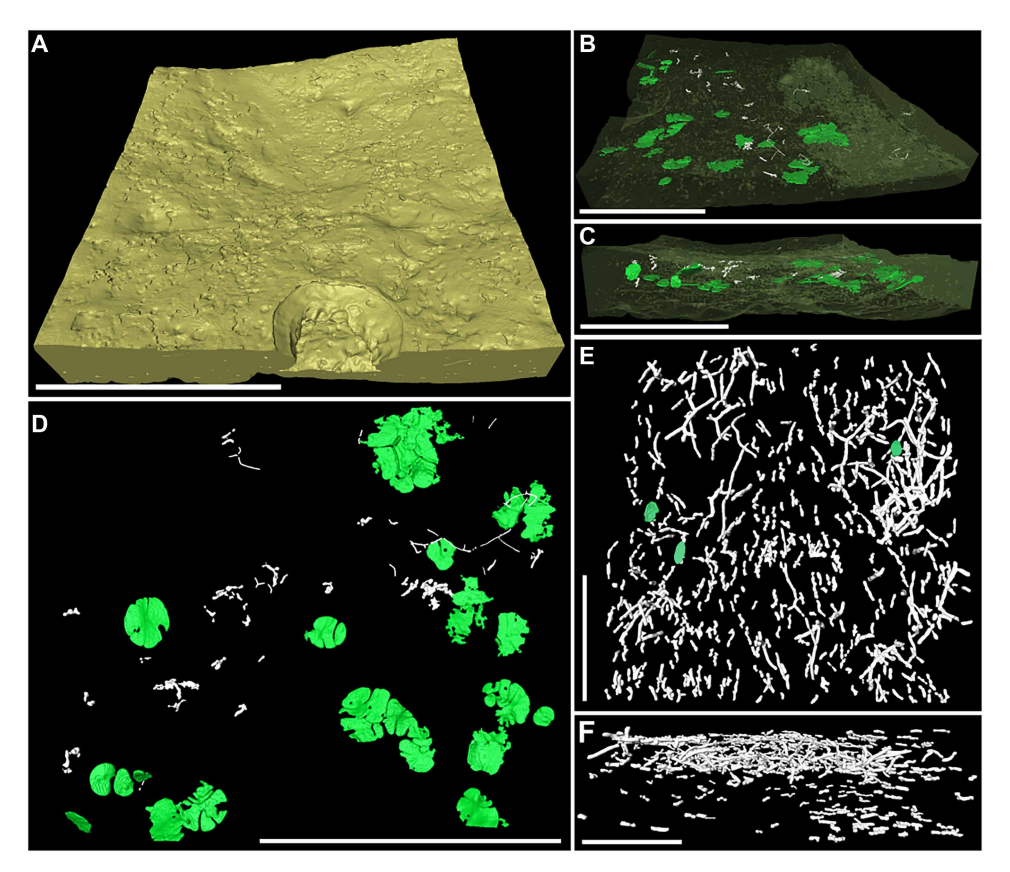


Fig. 3. SR-nanoCT 3D surface rendering of *S. nanum.* (**A**) External surface showing an open pore. (**B** and **C**) Translucent image of the same sample with the distribution of internal structures. (**D**) Internal photobiont cells (green) and hyphae (white). (**E**) Plane view of internal hyphae in another specimen with photobiont cells (green). (**F**) Perpendicular view of (E). Scale bars, 500 μm (A), 400 μm [(B) to (D)], 100 μm (E), and 50 μm (F).

This uniform orientation suggests that the thalli preserve their original growth mode, rather than representing fragments entangled during transport. Their arrangement, combined with their dorsiventral organization, suggests a prostrate, creeping habit, as previously suggested to *Spongiophyton minutissimum* (13). However, no attachment structures could be observed. The covering of the pores in *S. nanum* suggests that these structures were originally closed and later opened either during ontogeny or due to taphonomy. Raised borders and broken remnants further confirm this interpretation (Fig. 2, C and D). These features show analogies with the reported ontogeny of pseudocyphellae in modern lichens (16, 17). Although pores in *Spongiophyton* may not have been pseudocyphellae (11), they suggest a similar ontogeny and physiological role, such as gas exchange.

The observation of outer layers, especially on the poral, presumably upper surface, suggests that *Spongiophyton* originally had upper and lower cortex-like structures, which likely lost a recognizable cellular organization. This indicates a more stratified construction of the thallus than previously thought. The absence of these layers locally (Figs. 1M and 2F) may be due to decomposition or detachment before fossilization. Notably, similar features have been observed in taphonomic experiments on modern lichens subjected to compression and thermal alteration, where a layered anatomy persisted despite the loss of visible cellular detail (18).

The internal anatomy of *S. nanum* is highly reminiscent of modern lichens, with networks of anastomosing, dichotomously branching

hyphae that are similarly orientated relative to the surface of the thalli (Figs. 1 to 3 and fig. S1) and comparable micrometric diameter; the latter characteristic refutes affinities with actinobacteria, in which the filaments are usually <1 μm (8, 19). The presence of septa is reported in the hyphae of S. nanum, but they are not always conspicuous, likely due to preservation. Alternatively, these hyphae might have been irregularly septate. Putative reproductive structures (asci- or conidia-like features) associated with spore-like formations were also observed in the Devonian fossils (Fig. 1H), but they are noticeably smaller than the asci of modern lichens and their nature remains uncertain and should be further investigated.

Swollen hyphae are common components of endolithic lichens (20), although being also found in saxicolous forms (21). On the other hand, the large spherical cells are similar in size and morphology to the cells and cell packages of modern chlorophyte photobionts (22). Last, the hollow space bounded by the upper and lower layers in *Spongiophyton* (Figs. 1, L and M, and 2) was previously interpreted as the nonpreserved medulla of a lichen (11), but comparisons can also be drawn with modern lichens with hollow medullas, such as *Menegazzia* and *Hypogymnia* (23, 24). Overall, the anatomy of *S. nanum* shows notable similarities to modern lichenized fungi, but no feature provides clear evidence of affinities with either Ascomycota or Basidiomycota. This may indicate that it represents a particularly early diverging form of lichenized fungi with no representatives today.

Biomineralization

Chemical mappings of nano x-ray fluorescence (nanoXRF) (Fig. 4 and fig. S2) and energy-dispersive spectroscopy (EDS) (fig. S3, D and E) show numerous calcium-rich microparticles (~1 to 5 μ m) inside the organic material predominantly composing the fossilized remains of *S. nanum*, often arranged in layers closer to the outer surfaces. These Ca-rich particles are euhedral and show bipyramidal-prismatic morphologies (see the Supplementary Materials). Zn-rich microparticles are locally present as well (Fig. 4E). Unexpectedly, the hyphae are also preserved as a Ca-rich material (Fig. 4, A and D, and fig. S2A). Laser ablation inductively coupled plasma mass spectrometry (LA-ICPMS) and time-of-flight secondary ion mass spectrometry (ToF-SIMS) (fig. S5 and data S1) confirm the elevated Ca concentrations, while Fourier transform infrared (FTIR) spectroscopy, microFTIR, synchrotron x-ray diffraction (SR-XRD), and pair

distribution function (PDF) show their calcite mineralogy, possibly with a nanocrystalline structure (figs. S3 and S4, F, G, I, J, and M; see also the Supplementary Materials). Several pyrite peaks were identified in the diffractograms, and the presence of pyrite inclusions is evident (Fig. 4B and figs. S1, G and H, S3, A and D, and S4C).

Modern lichens are well-known to produce biominerals inside and on the surface of their thalli (25), the most common being calcium oxalate (CaOx), although calcite and other minerals were also reported (26). Unlike particles incorporated from the environment, oxalates and, sometimes, calcite can be biomineralized by lichens, even on noncalcareous substrates (26, 27). Despite their composition suggestive of low-magnesium calcite, the morphology and size of the calcite particles inside *S. nanum* are similar to bipyramidal and bipyramidal prismatic crystals of weddellite, a polymorph of CaOx observed in lichens (28) (see the Supplementary Materials). CaOx is also found

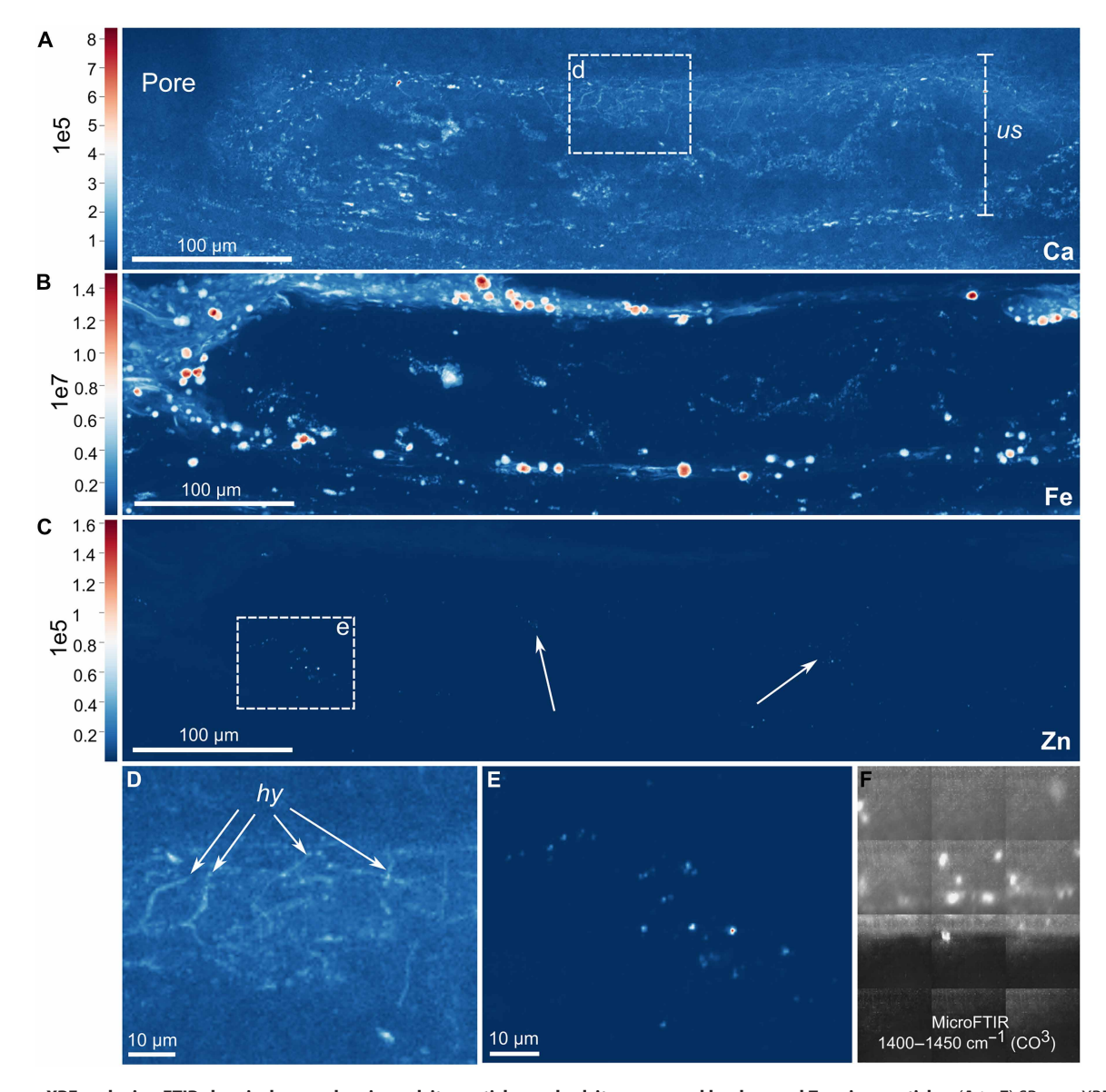


Fig. 4. SR-nanoXRF and microFTIR chemical maps showing calcite particles and calcite-preserved hyphae and Zn microparticles. (A to E) SR-nanoXRF of a longitudinal section of *S. nanum*, perpendicular to its surface, showing Ca (A), Fe (B), and Zn (C) maps, and respective insets for Ca (D) and Zn (E). (F) MicroFTIR map in the carbonate stretching vibration region. us, upper surface; hy, hyphae.

covering the walls of hyphae in modern lichens (29), in a notable similarity to the calcite-preserved hyphae here (Fig. 4, A and D). The fact that CaOx is no longer present is not unexpected because it is usually not preserved in the geological record (30). The occurrence of calcite microparticles (formerly, CaOx) forming layers (Fig. 4, A and F; and figs. S1, A and B, and S3D; see the Supplementary Materials) closer to the outer surfaces of S. nanum resembles CaOx layers deposited on the surface or even inside the upper cortex of lichens growing in environments with intense light (31). This is suggested to act as a protection against irradiance oxidative stress by increasing surface albedo of the thallus (31). To our knowledge, this is the first evidence of biomineralization in macroscopic fossil fungi and provides convincing complementary evidence for the lichen nature of these fossils. The local occurrence of Zn may also represent metal incorporation through biomineralization or particle entrapment (see the Supplementary Materials). The calcite-preserved hyphae, localized distribution of calcite microparticles, the lack of long-range order in calcite, and complete lack of calcite sediments/cements in the host rock all indicate a diagenetic origin after CaOx (please see the Supplementary Materials), rather than incorporation of calcite clasts before the final burial of the organism. On the other hand, pyrite inclusions are ubiquitous in kerogens and carbonaceous fossils, being simply a by-product of decomposition by sulfate-reducing bacteria. The pyrite inclusions differ in size, morphology, and distribution from the photobiont cells observed here.

Molecular composition of *Spongiophyton* carbonaceous matter

Elemental analysis (EA), organic petrography, x-ray photoelectron spectroscopy (XPS), and Rock-Eval show a high hydrogen and very low oxygen content for the fossilized remains of Spongiophyton. These results classify S. nanum organic matter as immature to slightly mature kerogen type I (Fig. 2, E and F, and data S1; see the Supplementary Materials). The high hydrogen content is reflected in the high aliphatic component in results from FTIR (fig. S6A), SR-XRD, PDF, and ¹³C solid-state nuclear magnetic resonance (¹³C SS-NMR), with aromatic and aliphatic fractions of 24 and 75%, respectively (data S1). Despite the low oxygen content, FTIR, XPS, and ¹³C SS-NMR reveal C-O, C=O, and O=C-O signals, with a lower content for the latter (data S1). Nitrogen functional groups appear in FTIR and ¹³C SS-NMR (fig. S6; see the Supplementary Materials), the former with a band near 1633 cm⁻¹ (C=O in amides), and a convoluted band near 1564 cm⁻¹ (C-N and N-H). Last, a FTIR band near 1513 cm⁻¹ is here assigned to secondary aromatic amines (see data S1 for detailed assignments) (32).

The nitrogen content in the Devonian fossils is substantial, around 2.7 wt % (C/N = 28). ToF-SIMS in negative ion spectrum confirms this high N content, with CN⁻ being the second largest peak (Fig. 5E and data S1). Other peaks can be attributed to N content, such as C_2N^- , CNO^- , C_3N^- , and C_5N^- . XPS also shows the presence of amines (~25%), pyridines (~24%), and pyrroles/amides (~24%) (Fig. 4B; see the Supplementary Materials). X-ray absorption near-edge structure (XANES) at the N K-edge corroborates the presence of pyridines and pyrroles (or pyridones) (fig. S6C). Alkylpyridines are among the most abundant pyrolysis products of the remains of *S. nanum* (Fig. 5F). Stable isotope measurements for $\delta^{15}N$ resulted in mean values of +3.48 per mil (‰; data S1).

These nitrogen and oxygen functionalities can show spatial variations in the fossilized thalli of *S. nanum*. MicroFTIR mapping shows

higher intensities of the C—N/N—H vibrations (1500 to 1600 cm⁻¹) toward the interior of the thalli, while the vibrational region of C=O (1700 to 1800 cm⁻¹) shows slightly higher intensities toward the outer surfaces (Fig. 5, C and D; and fig. S4, K to M), broadly corresponding to chemical differences seen by multispectral luminescence microscopy (fig. S6, D to F) and the location of the outer layers identified in thin sections.

Biomarker investigation of *Spongiophyton* revealed the presence of different hopanes for the fossil and host rocks. Among n-alkanes and waxes, the fossil extract and pyrolysate showed maxima at n- C_{15} and n- C_{14} , respectively, with a rapid decline toward higher homologs. This contrasts with the abundant odd-carbon numbered n-alkanes in the C_{21-37} range in the rock matrix reminiscent of cyanobacterial or algal sources (fig. S7; see the Supplementary Materials).

The classification of *Spongiophyton* carbonaceous matter as kerogen type I, with very low oxygen content, suggests that terrestrial plants are unlikely precursors. This type of kerogen is usually interpreted as resulting from lacustrine algal matter (33). *S. nanum* also shows lower contributions of C=O (relative to aliphatics) than most previous studies on plant leaves [e.g., (34); see also the Supplementary Materials] and lower oxygen and carboxyl/ester (relative to other carbonyls) content than early land plants (35).

The nitrogen compounds and their abundance also argue against affinities with early plants. More specifically, the amine-rich *Spongiophyton* kerogen indicates an original composition that was different from free-living algal and plant organic matter. More commonly studied immature kerogens often show much lower, or insignificant, amine content (36). The abundance of pyridines has, to our knowledge, never been observed before in fossil pyrolysates. Based on the uniform nature, simple distribution, and high relative abundance of the pyridines, as well as the absence of other major N-containing pyrolysis products, it is likely that the precursor was a polymer with a single type of reactive N moiety, such as chitin, or, more likely, chitosan after the degradation of chitin, without multiple different N functionalities as found in nucleic acids or proteins.

Higher oxygen-containing moieties toward the surface indicate the former presence of secondary metabolites, such as polyketides and phenolic compounds. Modern lichens can have spatial allocation of secondary metabolites, such as usnic acid concentrated in cortical areas (37). Small peaks in the ToF-SIMS positive ion spectra can be attributed to fragments of phenolic compounds (data S1). Spherical regions with high C—N/N—H intensities within the thallus of *S. nanum* (fig. S4E) may correspond to remnant pockets of chitin/chitosan-derived compounds or even be related to photobiont chemistry because amide moieties have been found in algaenan and alginite (38).

The $\delta^{15}N$ signatures may have implications for N sources and S. nanum photobionts. For instance, more positive values are observed in lichens growing in coastal areas, where they are influenced by marine breeze (39). Lichens growing in proximity to the sea show similar isotopic composition to particulate organic matter in the ocean (40), which is likely the case here (data S1), where the organisms had riparian habits but got transported into marine settings by the deltaic system. Moreover, lichens with N₂-fixing photobionts show slightly negative $\delta^{15}N$ values closer to 0‰ (41), reinforcing the interpretation of S. nanum photobionts as chlorophytes rather than cyanobacteria.

The different hopane (molecules produced by bacteria) homologs that occur in the matrix and the fossil indicates that specific bacteria degraded *Spongiophyton* biomass and/or lived in symbiosis with it (see the Supplementary Materials). The *n*-alkane composition of

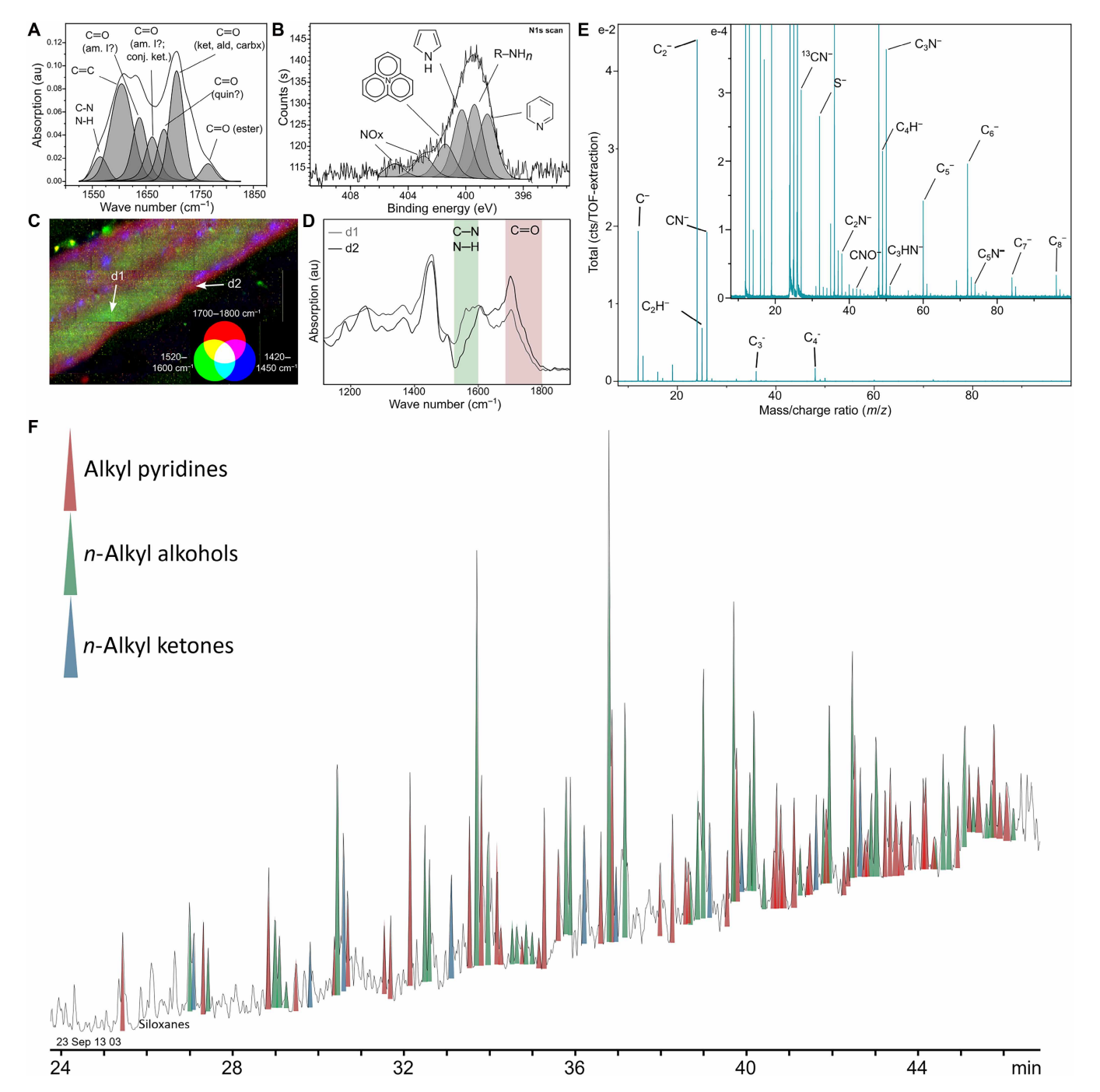


Fig. 5. Chemical composition of *S. nanum*. (A) deconvolution of transmission FTIR spectra in the region of C=O, C=C, and C=N. (B) Fitting of N1s XPS spectrum. (C) Superposed MicroFTIR chemical maps. (D) Spectra from the points arrowed in (C), showing differences in the C=N/N=H (green) and C=O (red) integrated areas. au, arbitrary units. (E) ToF-SIMS spectra in negative ion mode with peaks assigned to N-containing fragments. (F) GC-MS full-scan chromatogram of the polar fraction of *S. nanum* pyrolysate highlighting the relative abundances of straight-chain alkyl pyridines, alcohols, and ketones.

Spongiophyton is thus markedly different from the aquatic matrix and also from typical wax coatings of most land plants. Based on the high relative abundance of hopanes in *Spongiophyton*, it is likely that any wax coating and original fatty acids were aerobically degraded by bacteria before permanent burial. Intense aerobic reworking of the original lipid content is also consistent with low relative abundances of fungal and plant steranes (table S1) (42).

Spongiophyton lichenized nature and implications for terrestrialization

A lichenized structure in *Spongiophyton* was repeatedly proposed in the past (9-11) based on structure, especially the claimed presence of hyphae, gross morphology, ultrastructure, and isotopic composition. However, the hyphae were not illustrated in these works, and the observed δ^{13} C ranges proved to be not specific to lichens (14).

Notably, internal structures resembling hyphae have been illustrated in other occurrences of Spongiophyton around the world, including plate 1, figures 7 and 8 of (28); plate 124, figures 1 and 2 of (26); and text and figure 5D of (29), although their possible fungal nature was either dismissed or not addressed. The repeated occurrence of hyphal-like structures in Spongiophyton from geologically distinct environments speaks against a postmortem colonization by fungi decomposers, particularly given that these fossils are preserved as compressions rather than permineralization. A saprotrophic nature is further contradicted by the orientation of these hyphae to each other and to the surface, their preservation as calcite after CaOx, and their co-occurrence with CaOx microcrystal layers, which are all observations congruent with lichenization. If belonging to saprotrophic or parasitic fungi, then the hyphae would also show a random distribution, with radiating outward patterns from locations of colonization/infection. In summary, hyphae are neither rare nor random in Spongiophyton, and a saprophytic origin for them is highly unlikely.

The close association of the hyphae with the round cellular structures, here, interpreted as the symbiotic algae, also strongly refutes the hypothesis of the hyphae simply being some type of saprotrophic fungi. Similar round cellular structures have been reported in Spongiophyton from other geological units (11, 43), although their identity remains uncertain. In our material, the round cellular structures occur near the surface of the thalli, supporting their identification as symbiotic algae rather than degraded plant cells or large spores. These round cells and cell packages are isolated within the thalli of Spongiophyton, a clear departure from the closely packed structural or photosynthetic tissues of macroscopic red and green algae and bryophytes. A remaining alternative hypothesis would be that these round structures are remains of spherical minerals. However, the only spherical minerals inside Spongiophyton thalli are pyrite framboids, which are different in size and shape from the round cellular structures.

Adding to the extensive morphological information of Spongiophyton considered above, it is important to note that CaOx precipitation is not commonly observed in algae and bryophytes (44). Although CaOx may be common in vascular plants, Spongiophyton was clearly not a vascular plant, as demonstrated since the earliest studies. Furthermore, we report the presence of abundant nitrogen functional groups in this fossil, alongside with mass spectrometry (MS) data that show no compositional similarities to algal or plant matter. Previous works suggested higher nitrogen content based on simple EA (43). Chaloner et al. (43), however, cautioned against using these elemental results to infer an original chitin composition, arguing that graptolites have been shown to have high nitrogen content derived from scleroproteins. However, unless considering Spongiophyton as a metazoan, this concern is of no assistance to understanding Spongiophyton chemistry. Recently, Gaia et al. (15) attempted to investigate Spongiophyton fossils using EDS and FTIR. However, this attempt was flawed in multiple fundamental ways: (i) EDS is an unsuitable method for analyzing the chemistry of kerogen from carbonaceous fossil materials; (ii) their interpretations of EDS results are inconsistent; and (iii) absorption bands indicative of mineral content were misidentified as organic signals (see the Supplementary Materials). These issues misled them to claim that bryophyte and lichen affinities were equally plausible [page 9 of (15)].

Unlike *Spongiophyton*, other mid-Paleozoic fossils with proposed lichenized nature are known from isolated occurrences (8, 45). These

include Chlorolichenomycites devonicus and Cyanolichenomycites salopensis, both described on the basis of single specimens from the ~415-Ma Ditton Group and interpreted as charred fragments of heteromerous lichens (45). Their lichenized nature, however, has been subject to recent reconsideration [see supporting information in (6)]. The evidence for photobionts in these taxa consists of inclusions of framboidal pyrite or pseudomorphs after it. While it remains possible that these inclusions represent mineral artifacts rather than true photobionts, the heteromerous organization and other anatomical structures still provide strong support for a lichenized affinity. Winfrenatia reticulata from the Rhynie cherts (46, 47) represents another good lichen candidate [but see (7)]. Other (more dubious) Paleozoic possible lichens include the widespread nematophytes (48, 49) with their tubular constructions, which lack evidence of photobionts. A comprehensive review of putative fossil lichens is beyond the scope of this work, especially because thorough reviews are already available (2, 7). Nonetheless, we consider that *S. nanum* adds to a growing body of evidence that lichens may have been present among these early-middle Paleozoic enigmatic thalloid forms, highlighting the importance of cryptogamic covers during terrestrialization, especially at high latitudes (Figs. 6 and 7). After a ~250-Ma hiatus (7, 50), fossil lichens are found in Mesozoic and Cenozoic deposits, where their lichen nature is typically inferred from macroscopic morphology.

Our data provide strong evidence that *Spongiophyton* was one of the earliest lichenized macroscopic fungi and a dominant component of Devonian cryptogamic covers (Fig. 7). Regardless of its precise phylogenetic placement within fungi, our results confirm that the symbiosis between terrestrial heterotrophic fungi and photosynthetic eukaryotic algae has already evolved by the Early Devonian. These early lichens were widespread (Fig. 6) and commonly present in some Devonian successions (13). As other organisms in cryptogamic covers (2), lichens are stress-tolerant organisms (51) and can survive in harsh environments on Earth. As such, they may have acted as pioneer organisms in habitats still unsuitable for early land plant colonization, creating proto-soils (52) and biomass that would set the stage for the expansion of terrestrial plants and animals.

The evolution of complex terrestrial ecosystems was a long, stepwise, and phylogenetically diverse evolutionary process that may have spanned the Cambrian to the Late Devonian periods (53). This transformation is largely attributed to the emergence and diversification of land plants, especially vascular plants (i.e., tracheophytes), which enhanced weathering, soil formation and contributed to biogeochemical cycles (54). In contrast, although a critical role of lichens during terrestrialization has long been suggested, only isolated occurrences of lichens were described (45), the lichenized nature of which remains debated (6, 7).

Present-day cryptogamic covers contribute to biomass production, carbon and nitrogen cycles, and weathering processes (55, 56), accounting for ~7% of net primary production by terrestrial vegetation (55). The ability of *Spongiophyton* to biomineralize CaOx may have further influenced carbon and calcium cycles. The presence of widespread lichens by the Early Devonian could have also played a role in the environmental changes observed during this time. For instance, the expansion of weathering-active biota such as lichens and other cryptogams could have transiently enhanced the weatherability of silicate substrates, affecting sedimentation rates and nutrient fluxes to the oceans. These processes can promote anoxia and enhance carbon burial, leading to lower equilibrium pCO_2 . These

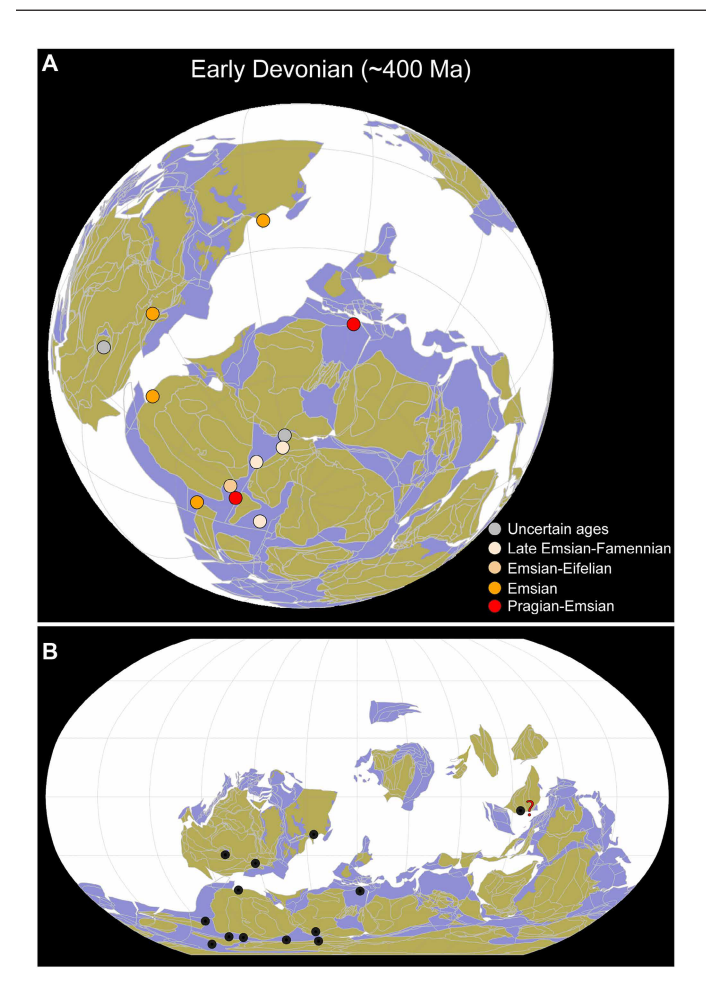


Fig. 6. Paleogeographic distribution of *Spongiophyton* **by the Early Devonian. (A)** 3D orthographic plot with color-coded occurrences and the plate reconstruction model from ref (84). Colors from red to pale orange represent older to younger relative ages. Grey-colored circles represent less well-defined ages. **(B)** Same distribution as in (A) but in a Robinson projection.

geochemical feedbacks were already related to environmental perturbations and extinction events in Middle-to-Late Devonian and are often linked to the rise of deep-rooting vascular plants (54).

Combined morphological, geochemical, and molecular approaches of other Paleozoic enigmatic thalloid fossils can provide additional data on the presence of lichens during specific stages of the terrestrialization process and even push back their presence to the upper Ordovician if *Nematothallus*-type cuticles represent lichenized fungi (2). *Spongiophyton*, now confidently identified as one of the oldest and most widespread lichens from the fossil record, illuminates the origins and composition of the first complex terrestrial ecosystems and the role of lichens within them.

MATERIALS AND METHODS

Fossil preparation

Selected fossil samples were processed in two different ways for chemical investigation. Here, we name these two sets of samples as demineralized *Spongiophyton* (DS) and demineralized *Spongiophyton* powder (DSP). The first is simply the isolation of the organic remains from the host rock by acid maceration (HCl and HF). The second is a step further on this process, where already DS fragments are ground in a mortar and subsequently demineralized again. This provided a better removal of mineral matter from deep within the organic cuticles. However, it is important to note that this process could not completely remove internal mineral particles given that some of them are close to 1 μ m in size (see the Biomineralization section). Powders of both DS and DSP were studied through EA, FTIR, ¹³C SS-NMR, lab-based XRD, SR-XRD, and PDF. None of the samples were treated with Schulze's solution because this procedure would markedly change the composition of the fossils.

On the other hand, intact demineralized and nondemineralized fragments were used for SR-nanoCT and XRD-CT. Only demineralized intact thalli were used for XPS and N K-edge XANES, which were intensely cleaned using ultrapure water before analysis. Sputtering was also used in these cases to further clean the fossil surfaces. Thin and polished sections were used for SR-micro- and nanoXRF, and lab-based microFTIR. For the ToF-SIMS analysis, we only used



Fig. 7. Artistic reconstruction of Spongiophyton during the Early Devonian in the high latitude depositional system of the Paraná Basin. Paleoart by J. Lacerda.

sample regions that were still embedded within the host rock. These portions of the fossils were then removed and broken perpendicular to the surface to expose clean regions within the thalli, avoiding contamination from the interface with the host rock.

SR nanotomography

Small samples (~300 $\mu m)$ for nanotomography were prepared using laser microdissection at the Cryogenic Sample Preparation Laboratory (LCRIO) facility of the Sirius synchrotron. These small samples were then glued to the tip of a short bristle or placed inside Kapton capillaries. At the dual imaging and diffraction (DIAD) beamline (Diamond Light Source), these samples were imaged in 180°, using unfiltered pink beam, a PCO.edge 5.5 detector scientific complementary metal-oxide-semiconductor (sCMOS), effective pixel size of 0.5 μm , and 5100 projections. Images were reconstructed using the filtered back projection algorithm available in the Savu python package, as well as using in-house–developed python pipelines from the Sirius computing team.

At the the micro and nanotomography beamline (MOGNO) (57), samples were imaged in the nanostation, with a 360° rotation angle, 22-keV quasimonochromatic cone beam, variable sample-detector distance (depending on sample size), a PCO Edge detector, and 2048 projections. The effective pixel size varied between 150 and 500 nm. The tomographic images were reconstructed using in-house-developed python pipelines together with Astra and Tomopy functionalities. We used the Avizo software for processing the reconstructed images.

Optical microscopy and organic petrography

Demineralized fragments of *Spongiophyton* were studied with a Leica LMD 7 laser microdissection microscope at the LCRIO facility (Sirius synchrotron). The laser microdissection coupled with this equipment was used for the preparation of very small samples for SR-nanoCT, ptychography, and XRD-CT.

Organic petrography was carried out on selected samples using polished blocks made with a cold-setting epoxy-resin mixture. The resulting sample pellets were ground and polished, in final preparation for microscopy, using an incident light Zeiss Axioimager II microscope system equipped with an ultraviolet (UV) light source and the Diskus-Fossil system. Fluorescence microscopy of organic matter was carried out using UV G 365-nm excitation with a 420-nm barrier filter to study fluorescence color variations of macerals. Random reflectance measurements were conducted under oil immersion (objective, ×50) following American Society for Testing and Materials (ASTM, 2014) methodology (58). The standard reference for reflectance measurement was yttrium aluminum garnet with a standard reflectance of 0.906% under oil immersion.

Scanning electron microscopy and EDS

One thin section was investigated in a Helios 5 PFIB CXE dual beam under the same proposal for ptychography. Secondary electron and backscattered electron images were acquired, and EA was performed with an energy dispersive spectrometer.

Elemental analysis

Acid-cleaned samples were investigated for C, N, O, and S content using an Exeter CE440 at Midwest Microlab.

FTIR spectroscopy

DS and DSP, as well as standards, were investigated using a Spectrum Two (PerkinElmer) spectrometer. KBr discs were prepared by mixing

1 mg of sample and 99 mg of KBr and pressed under 5 T for 5 min. KBr discs were examined not only after being prepared but also after 24 hours in the stove at 60°C to remove eventual adsorbed water. No significant changes were observed before and after dehydration for both fossil and standards, but we focused our analysis using spectra from the latter. In all cases, 100 acquisitions with a resolution of 4 cm⁻¹ were performed. The FTIR spectra were processed using the software OMNIC 9.9.473 and Fityk 1.3.1. We obtained a second derivative using the derivative function in OMNIC, through a Savitzky-Golay filter, 9 points, and a polynomial order of 3. The second derivative was used to check relative band positions, which were later used for deconvolution in the region of aliphatics (3000 to 2800 cm⁻¹) and carbonyls and aromatics (1800 to 1500 cm⁻¹).

Band assignments were based on available literature (mostly on kerogen and organic fossils) and are compiled in data S1. Some FTIR parameters were calculated, such as CHal/Ox (ratio of integrated area of 3000 to 2800/1800 to 1600) and CHal/C=O (3000 to 2800/1800 to 1700) for a broad comparison with the literature on FTIR studies of fossil plants (34, 59-64). However, we note that these parameters may not only reflect contributions from carbonyls and aromatics in the region of 1800 to 1600, and contributions from vibrations of other functional groups may alter these results. Additionally, it is also important to stress that any mineral impurity or water (adsorbed or in crystal structure) can also influence these parameters, as well as different processing methods used among studies, including methods of background removal and subsequent area integration. In sum, caution is necessary when interpreting FTIR spectra and its semiquantitative approaches for geological carbonaceous matter.

MicroFTIR

Chemical mapping of Spongiophyton with microFTIR was performed at the microstation of the IMBUIA beamline, using thin and polished sections. We used an Agilent Cary 670 spectrometer coupled with a Cary 620 microscope. MicroFTIR imaging was also performed at the IPANEMA laboratory using a Bruker Vertex 70v FT-IR spectrometer attached to a Bruker HYPERION 2000 FT-IR microscope, with an attenuated total reflection (ATR) system. Chemical maps in both cases were made in single image and panoramic modes using a focal plane array detector, which was periodically cooled with liquid nitrogen. At the infrared (IR) beamline (IMBUIA), the acquisition was made in reflectance mode using a 25× calibrated objective, while, at IPANEMA, the acquisition was performed using a micro-ATR objective. Multispectral images were acquired using varying accumulations, but mostly in the range of 256 and 512 scans. Before acquisition, background measurements were taken using the same number of scans. Some multispectral images acquired in reflectance mode had to be processed using a Kramers-Kronig transform. The data from IMBUIA beamline was processed using the Resolutions Pro software and Orange. Data from the IPANEMA lab was processed using the Quasar of the Orange suite. The general pipeline for processing the multispectral images included: (i) removal of the CO₂ vibrational region; (ii) truncation of the spectra for a better background subtraction; (iii) background subtraction using a rubber band baseline type; (iv) data normalization; and (v) plotting of chemical images based on integrated areas of spectral regions of interest, including 1400 to 1450, 1520 to 1600, and 1700 to 1800 cm⁻¹. Regarding the latter range, it is important to note that although C=O vibrations can contribute below this limit, we chose a slightly higher lower limit (1700 cm⁻¹) to

avoid contributions from other functional groups, such as amides, for instance.

SR-microXRF and nanoXRF

SR-XRF was performed at the CARNAÚBA beamline of the Sirius synchrotron (65). Thin and polished sections were mounted on beamline specific sample holders and carpins. These samples were scanned in the TARUMA station using a 9.75-keV monochromatic beam, with a beam size of 0.15 μm by 0.15 μm . Different programmed trajectories were used (i.e., size of scanned windows and resolution), and, in most cases, the regions of interest were imaged in panoramic mode, with spatial resolutions of 5, 0.5, and 0.1 μm . Map datasets were last processed using PyMca 5.6.3 (66).

Laboratory-based x-ray diffraction

Powder XRD was performed in a PANalytical diffractometer with Mo x-ray source. We used a tension of 40 kV and current of 40 mA. Diffractograms were acquired in the two-theta range of 2 to 50 for fossils, surrounding matrix, and other levels throughout the stratigraphy of the outcrop. Diffractograms were processed in the X'pert HighScore 3.0 software. Phase ID was based on open-source Crystallographic Information File (CIF) databases.

SR-XRD, XRD-CT, and PDF

Spongiophyton powders type DS and DSP, as well as standards, were analyzed at the 1-ID beamline of the Advanced Photon Source under proposal 80784. Samples for powder diffraction were placed inside 1- and 1.5-mm capillaries. All measurements were made using a photon energy of 71.676 keV, a sample detector distance of ~555 mm with a beam offset to get a higher q range (0.7 to 21.5 Å^{-1}). The diffraction patterns were collected using a flat GE amorphous Si detector. Calibration for the diffraction analysis was performed with a CeO₂ standard. Background measurement was carried out with empty capillaries and the same configuration as for samples. Detector images were processed in GSAS-II and included calibration, azimuthal integration (over a two-theta range of 1.1 to 34.52), and background removal. PDF was also performed in GSAS-II. The empirical formula used for the PDF of the fossils was C_{100.2}H₁₄₁N₃O₈S₂, which is based on our EA of the fossils. We also used $C_{118.3}H_{166.6}N_2O_{3.8}S$, which is based on EA and XPS, but both gave almost identical results.

For the XRD-CT measurements, two nondemineralized fossil fragments (~400 $\mu m)$ were scanned horizontally by the beam (size, 15 $\mu m)$ with 45 and 57 steps, 75 and 94 angles (angle step, 2.5 and 2), and 3 s of acquisition time at each point. The step size was the same as the beam size. The total number of diffractograms for each sample was 3375 and 5358. Angular projections were collected over a rotation of 180°. XRD-CT datasets were processed by in-house–developed algorithms included in the MIDAS package using MATLAB.

X-ray photoelectron spectroscopy

DS fragments were intensively cleaned with ultrapure water before XPS analysis. Samples were then mounted in the sample holder using carbon tape. Sputtering of the samples' surface was also used before the analysis, and depth profile was used to evaluate and remove spectra that, at the uppermost nanometric layers, will show higher oxygen levels due to atmosphere exposure. The measurements were performed in a K-Alpha X-ray Photoelectron Spectrometer System (Thermo Fisher Scientific) available at the National Nanotechnology Laboratory (LNNano, Brazilian Center for Research

in Energy and Materials-CNPEM). We used an electron flood gun for charge control. For the survey spectra, the conditions of analysis were as follow: 10 scans, 300-µm spot size, pass energy of 200.0 eV, 1.000 eV of energy step size, and 10 ms of dwell time. For the high-resolution spectra, the conditions were as follows: 10 scans, 300-µm spot size, pass energy of 50.0 eV, 0.10 eV of energy step size, and dwell time of 50 ms. The spectra were processed in CasaXPS version 2.3.25PR1.0, with the same fitting procedures for C1s and N1s as previously used by other authors (36, 67). Regarding the fitting of the N1s, we also stress that it is not possible to differentiate pyrroles from amides in the spectra.

Nitrogen K-edge XANES

Intact and clean fragments of *Spongiophyton* were studied at the IPE beamline of the SIRIUS synchrotron (68). Specimens were mounted in the sample holder using carbon tapes. N K-edge XANES measurements were made at the XPS station in total fluorescence yield, with 0.2 eV of resolution, 1 s of acquisition time, and spot size of 20 μm by 6 μm . Because we noticed beam damage after the first measurement, we decided to make only one acquisition at distinct positions in the samples. These spectra were then summed and processed in Athena (Demeter 0.9.26) software (69). A small correction in energy (-0.7 eV) was performed for all spectra on the basis of the amide peak from the chitin standard.

¹³C solid-state nuclear magnetic resonance

Around 100 mg of DS and DSP was analyzed in a Bruker Avance 400 spectrometer using a 7-mm rotor. The experiment was conducted in a Bruker Avance 400 spectrometer using a Jackobsen design probe head, operating at 400- and 100.5-MHz ^1H and ^{13}C , respectively. Typical experimental parameters were cross-polarization time of 1 ms, recycle delay of 1 s, ^1H and ^{13}C pulse lengths of 4.8 and 4.2 µs, respectively, and ^1H decoupling amplitude of $\gamma B_1/2\pi = 60$ kHz. Spectra were recorded at room temperature. Last, all ^{13}C NMR spectra were processed using the Fityk software.

Time-of-flight secondary ion mass spectrometry

A Spongiophyton fragment was removed from within the host rock before the analysis. The material was broken apart, and the clean internal perpendicular surface was analyzed in a TESCAN integrated ToF-SIMS system at the Centro Regional para o Desenvolvimento Tecnológico e Inovação of the Universidade Federal de Goiás. ToF-SIMS spectra were acquired in positive and negative ion modes using a xenon (Xe) focused ion beam, with current of 120 pA and tension varying between 15 and 30 keV. All mass spectra were processed in the software TOF-SIMS Explorer version 1.12.2.0. In the negative ion mode spectra, the calibration was performed using the C⁻, O⁻, CH⁻, C2⁻, S⁻, C3⁻, C4⁻, C5⁻, C6⁻, C7⁻, C8⁻, and C10⁻ peaks. In the positive mode spectra, the calibration was based on C^{+} , CH^{+} , CH_{3}^{+} , $C_{5}H_{9}^{+}$, $C_{6}H_{5}^{+}$, $C_{6}H_{9}^{+}$, $C_{6}H_{13}^{+}$, $C_{9}H_{7}^{+}$, OH_{2}^{+} , C_{3}^{+} , and Ca⁺ peaks. One important question to address here is the fact that the much larger abundance of low mass/charge ratio (m/z) fragments compared to previous works reflects the monoatomic ion source used here. Nevertheless, we can make broad comparisons with published ToF-SIMS of fossil materials, but we restrain ourselves from comparing relative intensities of the peaks.

Nitrogen isotopes

Nitrogen isotope ratios were analyzed on fossil organic matter and host sediments following published methods [e.g., (70, 71)]. Sample

powders (1 to 2 mg for fossil material and 10 to 20 mg for rock matrix) were weighed into tin capsules and combusted in an IsoLink (Thermo Fisher Scientific) elemental analyzer with a 5-s pulse of $\rm O_2$ and a He flow rate of 180 ml/min. The resulting gases were passed through a reduced copper column and Mg-perchlorate desiccant trap before being introduced to a Delta V Plus (Thermo Fisher Scientific) isotope ratio mass spectrometer via a Conflo IV continuous flow interface.

Raw isotopic data were corrected using a two-point calibration (72). Analytical blanks were subtracted from sample nitrogen data. Data are reported in delta notation relative to atmospheric N_2 . Samples N isotopic values were calculated using a series of standards, including USGS62 (caffeine, $\delta15N=20.17\%$) and a suite of internally calibrated standards: peat ($\delta15N=4.24\%$), sulfanilimide ($\delta15N=-2.86\%$), maple leaf ($\delta15N=1.33\%$), and linden leaf ($\delta15N=1.06\%$). Analytical precision is ~0.2%, based on replicate analyses of leaf standards.

Ptychography

The two-dimensional (2D) ptychographic experiment was performed at the CATERETÊ beamline (73), a coherent x-ray scattering dedicated beamline at Sirius synchrotron facility (74). The monochromatic beam, at 6 keV, was used for the measurements. A 5-µm pinhole was used to define the confined coherent illumination on the sample. The sample was scanned in the xy direction, with overleaping steps of 2 µm and with linear trajectory. The acquisition time per point was 150 ms, and the corresponding diffraction patterns were recorded with a PIMEGA 540D (PiTec, SP, Brazil) detector (55-µm pixel size and 3072×3072 pixels) placed in vacuum, 10 m from the sample. A total of 429 points were collected in a field of view of 44 μm (vertical) by 36 μm (horizontal). The 2D ptychographic reconstructions were performed using a combination of the relaxed averaged alternating reflections and alternating direction method of multipliers methods and implemented in Python by the LNLS Scientific Computing Group (not published). The resulting voxel size was 22.14 nm by 22.14 nm by 22.14 nm.

Laser ablation inductively coupled plasma mass spectrometry

One polished section with two longitudinally sectioned fragments were analyzed in an Applied Spectra RESOlution-SE excimer laser ablation system coupled to an Agilent 8900 mass spectrometer. GSD-1G, NIST610, calcite, pyrrhotite, and NIST1632D were used as reference materials. Other parameters were as follows: 24-µm spot size, repetition rate of 10 Hz, and fluence of 5 J/cm². Normalization was done as elements and total weight% calibrated with results from EA.

Point analyses were acquired in time-resolved sampling mode (peak hopping). Samples were ablated using a 24- μ m circular beam, a laser repetition rate of 10 Hz, and on-sample fluence of 5 J/cm². Ablation and background (gas blank) measurements, as well as washout times were set to 50 s each. By using a smoothing device (Squid) signal stability was enhanced (relative standard deviations < 2%). For quantification, to evaluate instrument drift and for quality assurance and quality control (QA/QC), a suite of reference materials was measured every 20 unknowns.

Data processing was performed with the iolite 4 software (75, 76) using the recently developed 3D Trace Elements data reduction scheme (77). The time-resolved LA-ICPMS spectra were standardized against 3D calibration surfaces, where the basaltic glass GSE-1G

[USGS; (78)] was selected as the primary calibrant. For P and Cl, the synthetic glass NIST-610 was chosen, while C and S were calibrated against in-house reference materials, calcite and pyrrhotite, respectively. In addition, the bituminous coal reference material NIST1632d was analyzed for quality control. Quantification of the data was achieved through normalization of the total element abundances to 74 wt %, on the basis of the results from EAs (excluding H, N, and O). Except for B, As, and Tl, measured concentrations of NIST-610 are in good agreement (<20%) with the GeoReM preferred values (79). For NIST1632d, the obtained concentrations are typically within 30% of the previously reported values (GeoReM database), the large discrepancy to the target for the remaining elements (Fe and Se) likely due to the heterogeneous nature of the analyzed material. A detailed summary of the instrument conditions and processing parameters is listed in data S1.

The correlation matrix with hierarchical clustering was obtained with RStudio using the corrplot library (T. Wei and V. Simko, 2024. R package "corrplot": Visualization of a correlation matrix; https://github.com/taiyun/corrplot). We used the dataset available in data S1. Rare earth elements (REE) and other trivalent (3+) elements were not included in the final plots, but we note that they all were strongly correlated with each other and slightly correlated with metals in the pyrite group, suggesting their presence in these sulfide minerals. Only correlations with P values of <0.05 were color coded in the correlation matrices.

Programmed pyrolysis Rock-Eval

Bulk sediment samples (~70 mg) were analyzed using programmed temperature heating. The pyrolysis stage (under N2) involved the initial isotemperature of 300°C for 3 min to release free hydrocarbons in the samples (S1, milligrams of HC per gram of rock), followed by ramping the temperature up 25°C/min to 650°C to release, through thermal cracking, hydrocarbons and the oxygen contained in pyrolizable kerogen (S2, milligrams of HC per gram of rock, and S3, milligrams of CO₂ per gram of rock, respectively). Samples were then automatically transferred to the oxidation oven and heated from 300° to 850°C at a heating rate of 20°C/min to measure the residual inert organic carbon [S4, milligrams of CO and CO2 per gram of rock and residual carbon (RC) wt %] and a portion of the mineral carbon (wt %). Total organic carbon (TOC; wt%) is quantified as the sum of the total quantity of organic matter released during pyrolysis (pyrolizable carbon wt %) and the oxidation step (RC wt %). The oxygen index is calculated by normalizing the quantity of the pyrolizable CO_2 (S3) to total organic carbon (S3/TOC × 100) and is proportional to the elemental O/C ratio of the kerogen while the hydrogen index is the ratio of (S2/TOC \times 100) and is proportional to H/C (80).

Biomarker analysis of solvent extracts and pyrolysates *Materials*

Solvents used were methanol (MeOH; OPTIMA grade ACS), dichloromethane (DCM; GC UNICHROM), and *n*-hexane (95% UNICHROM HPLC GC Pesticide grade). Glassware and aluminum foil were cleaned by combustion at 300°C for 9 hours. Metal appliances and agate mortar and pestle were washed with methanol and DCM before use.

Sample preparation and solvent extraction

During collection of *Spongiophyton* and sediment matrix samples, extreme care was taken to avoid contamination. The samples were

rapidly wrapped in combusted aluminum foil and only handled with cleaned tweezers. Hydrocarbons were analyzed in the Trace Biomarker Laboratory at the Australian National University using protocols developed for contamination-free analysis of biomarkers in lean bitumens and small fossil samples, including comprehensive, accumulatory laboratory system blanks that capture all steps in the process from specimen preparation to instrumental analysis. For biomarker analysis on the sediment matrix of Spongiophyton, surfaces were trimmed using a solvent-cleaned diamond wafering saw (Buehler Isomet 1000; Illinois, USA), and the sample interior was extracted, analyzed, and interpreted using protocols for the recognition and exclusion of contaminants (81, 82). The trimmed rock was ground to a <240 mesh powder using a Rocklabs iron puck mill. The mill was cleaned by rinsing with MeOH and DCM and by grinding annealed (600°C, 9 hours) quartz sand. Isolated Spongiophyton fossil material was inspected under a stereo microscope to ensure that it was devoid of attached sediment. Bitumens were extracted from the rock powder (15.64 g) and fossil (~20 mm²) via ultrasonic agitation in DCM for 30 min and allowed to remain in the solvent for a further 12 hours. Solvent was removed under a stream of purified nitrogen gas.

Pyrolysis

The solid residue of the extracted fossil was transferred to a silica glass pyrolysis tube (6 mm external diameter, 25 cm long, Choice Analytical). The tube was evacuated and flushed with N_2 gas several times using a vacuum line and then flame-sealed under vacuum. The sample-half of the tube was placed into a pyrolysis oven at 500°C, while the flame sealed end was exposed to room temperature to allow volatile pyrolysis products to condense instantly, protecting them against further thermal decomposition. The pyrolysis tube was removed from the oven after 10 min. The pyrolysate was extracted three times using 5 ml of DCM: MeOH (1:1 v/v) under ultrasonic agitation.

The solvent was removed under a stream of purified nitrogen gas and the pyrolysis products redissolved in ~2 ml of n-hexane. To hydrogenate double bonds formed during pyrolysis, a gentle stream of H_2 gas was bubbled through the solution for 5 min. Platinum(IV) oxide (0.2 mg) on charcoal (PtO₂, 10% on carbon, dry, Alfa Aesar) were added followed by another 10 min of H_2 supply under stirring. The system was tightly capped and allowed to react for 16 hours at room temperature (21°C) with stirring. The PtO₂ catalyst was removed by filtration over a silica gel microcolumn, and the hydrogenated products were collected using 3 ml of n-hexane and then 3 ml of DCM as eluents.

Fractionation of bitumens and pyrolysate

The matrix extract was fractionated into saturated, aromatic, and polar fractions using microcolumn chromatography over annealed (300°C, 12 hours) and dry packed silica gel (Silica Gel 60; 230 to 600 mesh; EM Science). Saturate hydrocarbons were eluted with 0.5 dead volumes (DV) of n-hexane, aromatic hydrocarbons with 2 DV of n-hexane:DCM (1:1 or 4:1 v/v), and polars with 3 DV of DCM:MeOH (1:1 v/v). The total lipid extract (TLE) of the fossil was not fractionated to avoid product loss. The fossil pyrolysate was fractionated into a combined saturated and aromatic fraction and a polar fraction.

As internal standard for full scan and selected iron recording (SIR) experiments, 150 ng of D10 (Pyrene- d_{10} , Chiron) was added to the saturated and aromatic fractions of the matrix extract and both fractions of the fossil pyrolysate. For metastable reaction monitoring

(MRM) experiments, 25 ng of D4 (d4- C_{29} - $\alpha\alpha\alpha$ -ethylcholestane; Chiron Laboratories AS) was added to the saturated hydrocarbon fraction of the matrix extract, the TLE of the fossil, and the saturated and aromatic fraction of the pyrolysate.

Gas chromatography-mass spectrometry

The gas chromatography (GC) was equipped with a 60-m DB-5 MS capillary column (inside diameter of 0.25 mm and film thickness of 0.25 μ m; Agilent JW Scientific, Agilent Technologies, Santa Clara, CA, USA), and helium was used as the carrier gas at a constant flow of 1 ml min $^{-1}$. Samples were injected in splitless mode into a Gerstel PTV injector at 60°C (held for 0.1 min) and heated at 260°C min $^{-1}$ to 300°C. The MS source was operated at 260°C in electron ionization mode at 70-eV ionization energy and 8000-V acceleration voltage. The MS source was operated at 260°C in electron ionization mode at 70-eV ionization energy and 8000-V acceleration voltage. For full-scan, SIR, and MRM analyses, the GC oven was programmed from 60°C (held for 4 min) to 315°C at 4°C min $^{-1}$, with total run time of 100 min. All samples were injected in *n*-hexane to avoid deterioration of chromatographic signals by FeCl₂ buildup in the MS ion source through use of halogenated solvents (83).

Saturated steranes, hopanes, and methyl hopanes were quantified using MRM M $^+$ \rightarrow 217.2, 191.2, and 205.2 precursor-product transitions, respectively. m/z values for the integration of aromatic steroids by SIR under magnet control are provided in table S1. All ratios and abundance proportions are reported uncorrected for differences in MS-response except where noted in table S1. Mass spectra were collected using full scan experiments at 1000 resolution and with a total cycle time of 1.28 s and are baseline corrected.

Supplementary Materials

The PDF file includes:

Supplementary Text Figs. S1 to S14 Table S1 Legend for data S1 References

Other Supplementary Material for this manuscript includes the following: Data S1

REFERENCES AND NOTES

- P. K. Strother, T. Servais, M. Vecoli, The effects of terrestrialization on marine ecosystems: The fall of CO₂. Geol. Soc. Lond. Spec. Publ. 339, 37–48 (2010).
- D. Edwards, L. Cherns, J. A. Raven, Could land-based early photosynthesizing ecosystems have bioengineered the planet in mid-Palaeozoic times? *Palaeontology* 58, 803–837 (2015).
- C. V. Rubinstein, P. Gerrienne, G. S. de la Puente, R. A. Astini, P. Steemans, Early Middle Ordovician evidence for land plants in Argentina (eastern Gondwana). New Phytol. 188, 365–369 (2010).
- G. Spaak, D. S. Edwards, C. B. Foster, A. Pagès, R. E. Summons, N. Sherwood, K. Grice, Environmental conditions and microbial community structure during the Great Ordovician Biodiversification Event; a multi-disciplinary study from the Canning Basin, Western Australia. Glob. Planet. Change 159, 93–112 (2017).
- M. Libertín, J. Kvaček, J. Bek, V. Žárský, P. Štorch, Sporophytes of polysporangiate land plants from the early Silurian period may have been photosynthetically autonomous. Nat Plants 4, 269–271 (2018).
- M. P. Nelsen, R. Lücking, C. K. Boyce, H. T. Lumbsch, R. H. Ree, No support for the emergence of lichens prior to the evolution of vascular plants. Geobiology 18, 3–13 (2020).
- R. Lücking, M. P. Nelsen, "Ediacarans, protolichens, and lichen-derived *Penicillium*," in *Transformative Paleobotany* (Elsevier, 2018), pp. 551–590; http://dx.doi.org/10.1016/ B978-0-12-813012-4.00023-1.
- R. Honegger, "Lichens and their allies past and present," in *Plant Relationships*, B. Scott, C. Mesarich, Eds. (The Mycota, 2023), pp. 133–183; https://link.springer.com/10.1007/978-3-031-16503-0_6.

SCIENCE ADVANCES | RESEARCH ARTICLE

- W. E. Stein, G. D. Harmon, F. M. Hueber, Spongiophyton from the Lower Devonian of North America reinterpreted as a lichen. Am. J. Bot. 80, 93 (1993).
- A. H. Jahren, S. Porter, J. J. Kuglitsch, Lichen metabolism identified in Early Devonian terrestrial organisms. *Geology* 31, 99–102 (2003).
- W. A. Taylor, C. Free, C. Boyce, R. Helgemo, J. Ochoada, SEM analysis of Spongiophyton interpreted as a fossil lichen. Int. J. Plant Sci. 165, 875–881 (2004).
- R. Kräusel, "Spongiophyton nov. gen. (Tallophita) und Haplostigma Seward (Pteridophyta) im UnterDevon von Parana," in Paleontologia Do Paraná: Volume Comemorativo Do 1.° Centenário Do Estado Do Paraná, F. Lange, Ed. (Comissão de Comemorações do Centenário do Paraná, Paraná, 1954), pp. 195–210.
- P. G. Gensel, W. G. Chaloner, W. H. Forbes, Spongiophyton from the late Lower Devonian of New Brunswick and Quebec, Canada. Palaeontology 34, 149–168 (1991).
- B. J. Fletcher, D. J. Beerling, W. G. Chaloner, Stable carbon isotopes and the metabolism of the terrestrial Devonian organism Spongiophyton. Geobiology 2, 107–119 (2004).
- G. Gaia, V. R. Ribeiro, R. P. Ghilardi, F. N. Sousa, M. P. Llopart, F. Ricardi-Branco, Chemical and elementary characterization of *Spongiophyton nanum*: Understanding the phylogeny, paleoenvironment, and fossilization processes of an enigmatic flora. *Rev. Palaeobot. Palynol.* 316, 104943 (2023).
- M. E. Hale, Pseudocyphellae and pored epicortex in the parmeliaceae: Their delimitation and evolutionary significance. *Lichenologist* 13, 1–10 (1981).
- C. A. Zanetti, S. B. Barbosa, S. A. Adachi, M. P. Marcelli, Pseudocyphellae ontogeny and thallus anatomy in species of *Punctelia* Krog (Parmeliaceae, lichenized Ascomycota). *Acta Bot. Bras.* 31, 51–57 (2017).
- A. M. F. Tomescu, R. W. Tate, N. G. Mack, V. J. Calder, "Simulating fossilization to resolve the taxonomic affinities of thalloid fossils in Early Silurian (ca. 425 Ma) terrestrial assemblages," in *Biology of Lichens: Symbiosis, Ecology, Environmental Monitoring, Systematics, Cyber Applications*, T. Nash III, Ed. (Cambridge Univ. Press, 2010), pp. 183–190.
- R. Honegger, "Fossil lichens from the Lower Devonian and their bacterial and fungal epi-and endobionts," in *Biodiversity and Ecology of Fungi, Lichens, and Mosses* (Austrian Academy of Sciences, 2018), pp. 547–564.
- E. Kushnir, A. Tietz, M. Galun, "Oil hyphae" of endolithic lichens and their fatty acid composition. Protoplasma 97, 47–60 (1978).
- W. B. Sanders, C. Ascaso, J. Wierzchos, Physical interactions of two rhizomorph-forming lichens with their rock substrate. *Bot. Acta* 107, 432–439 (1994).
- V. Veselá, V. Malavasi, P. Škaloud, A synopsis of green-algal lichen symbionts with an emphasis on their free-living lifestyle. *Phycologia* 63, 317–338 (2024).
- J. W. Bjerke, Revision of the lichen genus Menegazzia in Japan, including two new species. Lichenologist 36, 15–25 (2004).
- E. S. Hansen, B. Mccune, The lichen genus Hypogymnia in Greenland. Folia Cryptogam. Est. 47, 13–20 (2010).
- C. Ascaso, Lichens on rock substrates: Observation of the biomineralization processes. *Bibl. Lichenol.* 75, 127–135 (2000).
- C. Ascaso, L. G. Sancho, C. Rodriguez-Pascual, The weathering action of saxicolous lichens in maritime Antarctica. *Polar Biol.* 11, 33–39 (1990).
- 27. J. A. Erdman, L. P. Gough, R. W. White, Calcium Oxalate as source of high ash yields in the terricolous lichen *Parmelia chlorochroa*. *Bryologist* **80**, 334 (1977).
- O. V. Frank-Kamenetskaya, G. Y. Ivanyuk, M. S. Zelenskaya, A. R. Izatulina,
 A. O. Kalashnikov, D. Y. Vlasov, E. I. Polyanskaya, Calcium oxalates in lichens on surface of apatite-nepheline ore (Kola Peninsula, Russia). *Minerals* 9, 656 (2019).
- V. Souza-Egipsy, J. Wierzchos, J. V. García-Ramos, C. Ascaso, Chemical and ultrastructural features of the lichen-volcanic/sedimentary rock interface in a semiarid region (Almería, Spain). *Lichenologist* 34, 155–167 (2002).
- E. J. Baran, P. V. Monje, "Oxalate biominerals," in *Biomineralization* (Wiley, 2008); vol. 4, pp. 219–254; https://onlinelibrary.wiley.com/doi/10.1002/9780470986325.ch7.
- P. Modenesi, M. Piana, D. Pinna, Surface features in *Parmelia sulcata* (Lichenes) thalli growing in shaded or exposed habitats. *Nova Hedwigia* 66, 535–547 (1998).
- R. M. Silverstein, F. X. Webster, D. J. Kiemle, D. L. Bryce, Spectrometric Identification of Organic Compounds (John Wiley & Sons Ltd., ed. 8, 2014); www.wiley.com/en-us/Spect rometric+Identification+of+Organic+Compounds%2C+8th+Edition-p-9780470616376.
- B. P. Tissot, D. H. Welte, Petroleum Formation and Occurrence (Springer, 1984); http://link. springer.com/10.1007/978-3-642-87813-8.
- M. A. Lafuente Diaz, G. M. Del Fueyo, J. A. D'Angelo, M. A. Carrizo, How much does Chemotaxonomy help to resolve the overrepresented *Cycadolepis* Saporta (Bennettitales)? A case study of the Cretaceous of Patagonia, Argentina. *Rev. Palaeobot. Palynol.* 293, 104489 (2021).
- G. D. Abbott, I. W. Fletcher, S. Tardio, E. Hack, Exploring the geochemical distribution of organic carbon in early land plants: A novel approach. *Philos. Trans. R. Soc. B Biol. Sci.* 373, 20160499 (2018).
- S. R. Kelemen, M. Afeworki, M. L. Gorbaty, M. Sansone, P. J. Kwiatek, C. C. Walters, H. Freund, M. Siskin, A. E. Bence, D. J. Curry, M. Solum, R. J. Pugmire, M. Vandenbroucke, M. Leblond, F. Behar, Direct characterization of kerogen by X-ray and solid-state ¹³C nuclear magnetic resonance methods. *Energy Fuels* 21, 1548–1561 (2007).

- P. Le Pogam, B. Legouin, A. Geairon, H. Rogniaux, F. Lohézic-Le Dévéhat, W. Obermayer,
 J. Boustie, A. C. Le Lamer, Spatial mapping of lichen specialized metabolites using
 LDI-MSI: Chemical ecology issues for *Ophioparma ventosa*. Sci. Rep. 6, 37807 (2016).
- H. I. Petersen, P. Rosenberg, H. P. Nytoft, Oxygen groups in coals and alginite-rich kerogen revisited. *Int. J. Coal. Geol.* 74, 93–113 (2008).
- Y. II Lee, H. S. Lim, H. II Yoon, Carbon and nitrogen isotope composition of vegetation on King George Island, maritime Antarctic, *Polar Biol.* 32, 1607–1615 (2009).
- A. H. L. Huiskes, H. T. S. Boschker, D. Lud, T. C. W. Moerdijk-Poortvliet, Stable isotope ratios as a tool for assessing changes in carbon and nutrient sources in antarctic terrestrial ecosystems. *Plant Ecol.* 182, 79–86 (2006).
- P. Hietz, W. Wanek, R. Wania, N. M. Nadkarni, Nitrogen-15 natural abundance in a montane cloud forest canopy as an indicator of nitrogen cycling and epiphyte nutrition. *Oecologia* 131, 350–355 (2002).
- I. Bobrovskiy, S. W. Poulton, J. M. Hope, J. J. Brocks, Impact of aerobic reworking of biomass on steroid and hopanoid biomarker parameters recording ecological conditions and thermal maturity. *Geochim. Cosmochim. Acta* 364, 114–128 (2024).
- 43. W. G. Chaloner, M. K. Mensah, M. D. Crane, Non-vascular land plants from the Devonian of Ghana. *Palaentology* **17**, 925–947 (1974).
- 44. H. Arnott, F. Pautard, "Calcification in plants," in *Biological Calcification*, H. Schraer, Ed. (Appleton-Century-Crofts, 1970), pp. 375–440.
- R. Honegger, D. Edwards, L. Axe, The earliest records of internally stratified cyanobacterial and algal lichens from the Lower Devonian of the Welsh Borderland. New Phytol. 197, 264–275 (2013).
- T. N. Taylor, H. Hass, W. Remy, H. Kerp, The oldest fossil lichen. Nature 378, 244–244 (1995)
- I. V. Karatygin, N. S. Snigirevskaya, S. V. Vikulin, The most ancient terrestrial lichen Winfrenatia reticulata: A new find and new interpretation. Paleontol. J. 43, 107–114 (2009).
- D. Edwards, L. Axe, R. Honegger, Contributions to the diversity in cryptogamic covers in the mid-Palaeozoic: Nematothallus revisited. Bot. J. Linn. Soc. 173, 505–534 (2013).
- D. Edwards, R. Honegger, L. Axe, J. L. Morris, Anatomically preserved Silurian "nematophytes" from the Welsh Borderland (UK). Bot. J. Linn. Soc. 187, 272–291 (2018).
- Q. Yang, Y. Wang, R. Lücking, T. H. Lumbsch, Z. Du, Y. Chen, M. Bai, D. Ren, J. Wei, H. Li, Y. Wang, X. Wei, The Jurassic epiphytic macrolichen *Daohugouthallus* reveals the oldest lichen-plant interaction in a Mesozoic forest ecosystem. *IScience* 26, 105770 (2023).
- I. Kranner, R. Beckett, A. Hochman, T. H. Nash, Desiccation-tolerance in lichens: A review. Bryologist 111, 576–593 (2008).
- R. L. Mitchell, C. Strullu-Derrien, P. Kenrick, Biologically mediated weathering in modern cryptogamic ground covers and the early paleozoic fossil record. *J. Geol. Soc. London* 176, 430–439 (2019).
- P. Gerrienne, T. Servais, M. Vecoli, Plant evolution and terrestrialization during Palaeozoic times—The phylogenetic context. Rev. Palaeobot. Palynol. 227, 4–18 (2016).
- T. J. Algeo, S. E. Scheckler, Terrestrial-marine teleconnections in the Devonian: Links between the evolution of land plants, weathering processes, and marine anoxic events. *Philos. Trans. R. Soc. Lond. B Biol. Sci.* 353, 113–130 (1998).
- W. Elbert, B. Weber, S. Burrows, J. Steinkamp, B. Büdel, M. O. Andreae, U. Pöschl, Contribution of cryptogamic covers to the global cycles of carbon and nitrogen. *Nat. Geosci.* 5, 459–462 (2012).
- P. Porada, B. Weber, W. Elbert, U. Pöschl, A. Kleidon, Estimating impacts of lichens and bryophytes on global biogeochemical cycles. Global Biogeochem. Cycles 28, 71–85 (2014).
- N. L. Archilha, G. R. Costa, G. R. B. Ferreira, G. B. Z. L. Moreno, A. S. Rocha, B. C. Meyer, A. C. Pinto, E. X. S. Miqueles, M. B. Cardoso, H. Westfahl Jr., MOGNO, the nano and microtomography beamline at Sirius, the Brazilian synchrotron light source. *J. Phys. Conf. Ser.* 2380, 012123 (2022).
- ASTM D7708-14, Standard Test Method for Microscopical Determination of the Reflectance of Vitrinite Dispersed in Sedimentary Rocks (Advancing Standards Transforming Markets, 2014); https://store.astm.org/d7708-14.html.
- E. L. Zodrow, J. A. D'Angelo, M. Mastalerz, C. J. Cleal, D. Keefe, Phytochemistry of the fossilized-cuticle frond *Macroneuropteris macrophylla* (Pennsylvanian seed fern, Canada). *Int. J. Coal Geol.* 84, 71–82 (2010).
- J. A. D'Angelo, E. L. Zodrow, M. Mastalerz, Compression map, functional groups and fossilization: A chemometric approach (Pennsylvanian neuropteroid foliage, Canada). *Int. J. Coal Geol.* 90–91, 149–155 (2012).
- J. A. D'Angelo, L. B. Escudero, W. Volkheimer, E. L. Zodrow, Chemometric analysis of functional groups in fossil remains of the *Dicroidium* flora (Cacheuta, Mendoza, Argentina): Implications for kerogen formation. *Int. J. Coal Geol.* 87, 97–111 (2011).
- J. A. D'Angelo, E. L. Zodrow, Fossil cutin of *Johnstonia coriacea* (Corystospermaceae, Upper Triassic, Cacheuta, Argentina). *Int. J. Coal Geol.* 189, 70–74 (2018).
- M. A. Lafuente Diaz, J. A. D'angelo, G. M. Del Fueyo, E. L. Zodrow, Fossilization model for Squamastrobus tigrensis foliage in a volcanic-ash deposit: Implications for preservation and taphonomy (Podocarpaceae, Lower Cretaceous, Argentina). Palaios 33, 323–337 (2018).

SCIENCE ADVANCES | RESEARCH ARTICLE

- M. A. Lafuente Diaz, J. A. D'Angelo, G. M. Del Fueyo, M. A. Carrizo, FTIR spectroscopic features of the pteridosperm *Ruflorinia orlandoi* and host rock (Springhill Formation, Lower Cretaceous, Argentina). J. South Am. Earth Sci. 99, 102520 (2020).
- H. C. N. Tolentino, M. M. Soares, C. A. Perez, F. C. Vicentin, D. B. Abdala, D. Galante, V. D. C. Teixeira, D. H. C. de Araújo, H. Westfahl, CARNAÚBA: The coherent x-ray nanoprobe beamline for the brazilian synchrotron SIRIUS/LNLS. J. Phys. Conf. Ser. 849, 012057 (2017).
- V. A. Solé, E. Papillon, M. Cotte, P. Walter, J. Susini, A multiplatform code for the analysis of energy-dispersive X-ray f luorescence spectra. Spectrochim. Acta B At. Spectrosc. 62, 63–68 (2007)
- Q. Wang, Q. Liu, Z. Wang, H. Liu, J. Bai, X-ray photoelectron spectroscopy investigation of nitrogen transformation in Chinese oil shales during pyrolysis. Oil Shale 34, 129–145 (2017).
- B. C. Meyer, T. C. R. Rocha, S. A. L. Luiz, A. Clarindo Pinto, H. Westfahl, "Simulation and optimization of the Sirius IPE soft x-ray beamline," in *Advances in Computational Methods* for X-Ray Optics IV, K. Sawhney, O. Chubar, Eds. (SPIE, 2017), vol. 10388, p. 13.
- B. Ravel, M. Newville, ATHENA, ARTEMIS, HEPHAESTUS: Data analysis for X-ray absorption spectroscopy using IFEFFIT. J. Synchrotron Radiat. 12, 537–541 (2005).
- B. W. Johnson, C. Mettam, S. W. Poulton, Combining nitrogen isotopes and redox proxies strengthens paleoenvironmental interpretations: Examples from neoproterozoic snowball Earth sediments. Front. Earth Sci. 10, 745830 (2022).
- M. A. Kipp, E. E. Stüeken, C. A. E. Strömberg, W. H. Brightly, V. M. Arbour, B. Erdei, R. S. Hill, K. R. Johnson, J. Kvaček, J. C. McElwain, I. M. Miller, M. Slodownik, V. Vajda, R. Buick, Nitrogen isotopes reveal independent origins of N₂-fixing symbiosis in extant cycad lineages. *Nat. Ecol. Evol.* 8, 57–69 (2024).
- T. B. Coplen, W. A. Brand, M. Gehre, M. Gröning, H. A. J. Meijer, B. Toman,
 R. M. Verkouteren, New guidelines for δ 13 C measurements. *Anal. Chem.* 78, 2439–2441 (2006)
- F. Meneau, A. R. Passos, P. R. A. F. Garcia, P. Vinaches, L. B. Manoel, T. A. Kalile, J. P. Zerba, G. L. M. P. Rodrigues, E. Miqueles, G. Baraldi, J. Polli, B. C. Meyer, S. A. L. Luiz, C. Polo, Cateretê: The coherent X-ray scattering beamline at the fourth-generation synchrotron facility SIRIUS. Acta Crystallogr. A Found. Adv. 77, C283–C283 (2021).
- L. Liu, N. Milas, A. H. C. Mukai, X. R. Resende, F. H. De Sá, The sirius project. J. Synchrotron Radiat. 21, 904–911 (2014).
- C. Paton, J. Hellstrom, B. Paul, J. Woodhead, J. Hergt, Iolite: Freeware for the visualisation and processing of mass spectrometric data. J. Anal. At. Spectrom 26, 2508–2518 (2011).
- J. A. Petrus, D. M. Chew, M. I. Leybourne, B. S. Kamber, A new approach to laser-ablation inductively-coupled-plasma mass-spectrometry (LA-ICP-MS) using the flexible map interrogation tool 'Monocle'. Chem. Geol. 463, 76–93 (2017).
- B. Paul, J. Petrus, D. Savard, J. Woodhead, J. Hergt, A. Greig, C. Paton, P. Rayner, Time resolved trace element calibration strategies for LA-ICP-MS. J. Anal. At. Spectrom 38, 1995–2006 (2023).
- M. Guillong, K. Hametner, E. Reusser, S. A. Wilson, D. Günther, Preliminary characterisation of new glass reference materials (GSA-1G, GSC-1G, GSD-1G and GSE-1G) by laser ablation-inductively coupled plasma-mass spectrometry using 193 nm, 213 nm and 266 nm wavelengths. *Geostand. Geoanal. Res.* 29, 315–331 (2005).
- K. P. Jochum, U. Nohl, K. Herwig, E. Lammel, B. Stoll, A. W. Hofmann, GeoReM: A new geochemical database for reference materials and isotopic standards. *Geostand. Geoanal.* Res. 29, 333–338 (2005).
- E. Lafargue, F. Marquis, D. Pillot, Rock-Eval 6 applications in hydrocarbon exploration, production, and soil contamination studies. *Rev. Inst. Fr. Pét.* 53, 421–437 (1998).
- J. J. Brocks, Millimeter-scale concentration gradients of hydrocarbons in Archean shales: Live-oil escape or fingerprint of contamination? *Geochim. Cosmochim. Acta* 75, 3196–3213 (2011).
- J. J. Brocks, E. Grosjean, G. A. Logan, Assessing biomarker syngeneity using branched alkanes with quaternary carbon (BAQCs) and other plastic contaminants. Geochim. Cosmochim. Acta 72, 871–888 (2008).
- J. J. Brocks, J. M. Hope, Tailing of chromatographic peaks in GC-MS caused by interaction of halogenated solvents with the ion source. J. Chromatogr. Sci. 52, 471–475 (2014).
- A. S. Merdith, S. E. Williams, A. S. Collins, M. G. Tetley, J. A. Mulder, M. L. Blades, A. Young, S. E. Armistead, J. Cannon, S. Zahirovic, R. D. Müller, Extending full-plate tectonic models into deep time: Linking the neoproterozoic and the phanerozoic. *Earth Sci. Rev.* 214, 103477 (2021).
- 85. E. Pereira, "Evolução tectono-sedimentar do intervalo Ordoviciano-Devoniano da Bacia do Paraná," thesis, Universidade de São Paulo (2000).
- B. Becker-Kerber, G. L. Osés, J. F. Curado, M. De Almeida Rizzutto, I. D. Rudnitzki,
 G. R. Romero, S. Y. Onary-Alves, V. G. Benini, D. Galante, F. Rodrigues, P. V. Buck,
 E. C. Rangel, R. P. Ghilardi, M. L. A. F. Pacheco, Geobiological and diagenetic insights from Malvinokaffric Devonian biota (Chapada group, Paraná Basin, Brazil): Paleobiological and paleoenvironmental implications. *Palaios* 32, 238–249 (2017).
- 87. J. H. G. Melo, "The malvinokaffric realm in the devonian of Brazil," in *Devonian of the World: Proceedings of the 2nd International Symposium on the Devonian System*,

- N. J. McMillam, A. F. Embry, D. J. Glass, Eds. (Canadian Society of Petroleum Geologists, 1988), vol. 14, pp. 669–703.
- Y. Grahn, P. M. Mauller, E. Pereira, S. Loboziak, Palynostratigraphy of the Chapada Group and its significance in the Devonian stratigraphy of the Paraná Basin, south Brazil. J. South Am. Earth Sci. 29, 354–370 (2010).
- Y. Grahn, E. Pereira, S. Bergamaschi, Silurian and lower Devonian chitinozoan biostratigraphy of the Paraná Basin in Brazil and Paraguay. *Palynology* 24, 147–176 (2000)
- D. Sedorko, R. G. Netto, S. M. Scheffler, R. S. Horodyski, E. P. Bosetti, R. P. Ghilardi, P. M. Mauller, M. R. de Vargas, R. Videira-Santos, R. C. da Silva, L. Myzynski-Junior, Paleoecologic trends of Devonian Malvinokaffric fauna from the Paraná Basin as evidenced by trace fossils. J. South Am. Earth Sci. 109, 103200 (2021).
- R. Kräusel, B. Venkatachala, Devonische Spongiophytaceen aus Ost- und West-Asien. Senck. Lethaea 47. 215–251 (1966).
- F. M. Michel, J. MacDonald, J. Feng, B. L. Phillips, L. Ehm, C. Tarabrella, J. B. Parise,
 R. J. Reeder, Structural characteristics of synthetic amorphous calcium carbonate. *Chem. Mater.* 20, 4720–4728 (2008).
- 93. M. Bačkor, S. Loppi, Interactions of lichens with heavy metals. Biol. Plant. 53, 214–222 (2009).
- 94. V. Krajanová, Discoveries and identification methods of metal oxalates in lichens and their mineral associations: A review of past studies and analytical options for lichenologists. *Fungal Biol. Rev.* **43**, 100287 (2023).
- M. Malekhosseini, H. J. Ensikat, V. E. McCoy, T. Wappler, M. Weigend, L. Kunzmann, J. Rust, Traces of calcium oxalate biomineralization in fossil leaves from late Oligocene maar deposits from Germany. Sci. Rep. 12, 15959 (2022).
- M. T. Suekuni, P. R. Craddock, J. T. Douglas, A. E. Pomerantz, A. M. Allgeier, Critical practices for the preparation and analysis of Kerogen. *Energy Fuels* 36, 8828–8843 (2022).
- X. H. Guan, Y. Liu, D. Wang, Q. Wang, M. S. Chi, S. Liu, C. G. Liu, Three-dimensional structure of a Huadian oil shale Kerogen model: An experimental and theoretical study. *Energy Fuels* 29, 4122–4136 (2015).
- M. N. Siddiqui, M. F. Ali, J. Shirokoff, Use of X-ray diffraction in assessing the aging pattern of asphalt fractions. Fuel 81, 51–58 (2002).
- A. M. Orendt, I. S. O. Pimienta, S. R. Badu, M. S. Solum, R. J. Pugmire, J. C. Facelli,
 D. R. Locke, K. W. Chapman, P. J. Chupas, R. E. Winans, Three-dimensional structure of the siskin green river oil shale kerogen model: A comparison between calculated and observed properties. *Energy Fuels* 27, 702–710 (2013).
- P. Leinweber, J. Kruse, F. L. Walley, A. Gillespie, K. U. Eckhardt, R. I. R. Blyth, T. Regier, Nitrogen K-edge XANES – An overview of reference compounds used to identify "unknown" organic nitrogen in environmental samples. *J. Synchrotron Radiat.* 14, 500–511 (2007).
- Y. Zubavichus, M. Zharnikov, A. Shaporenko, O. Fuchs, L. Weinhardt, C. Heske, E. Umbach, J. D. Denlinger, M. Grunze, Soft X-ray induced decomposition of phenylalanine and tyrosine: A comparative study. Chem. A Eur. J. 108, 4557–4565 (2004).
- 102. G. D. Cody, H. Ade, C. M. O. D. Alexander, T. Araki, A. Butterworth, H. Fleckenstein, G. Flynn, M. K. Gilles, C. Jacobsen, A. L. D. Kilcoyne, K. Messenger, S. A. Sandford, T. Tyliszczak, A. J. Westphal, S. Wirick, H. Yabuta, Quantitative organic and light-element analysis of comet 81P/Wild 2 particles using C-, N-, and O-μ-XANES. *Meteorit. Planet. Sci.* 43, 353–365 (2008).
- S. R. Kelemen, M. L. Gorbaty, P. J. Kwiatek, Quantification of nitrogen forms in argonne premium coals. *Energy Fuels* 8, 896–906 (1994).
- W. M. K. Matsumura, M. Di Pasquo, R. lannuzzi, E. P. Bosetti, "Plant diversification through the Devonian in Brazil," in *Brazilian Paleofloras: From Paleozoic to Holocene* (Springer Nature, 2024), pp. 1–79.
- 105. D. Sedorko, E. P. Bosetti, R. P. Ghilardi, L. José, M. Júnior, R. C. Silva, S. M. Scheffler, Paleoenvironments of a regressive Devonian section from Paraná Basin (Mato Grosso do Sul state) by integration of ichnologic, taphonomic and sedimentologic analyses. *Braz. J. Geol.* 48, 805–820 (2018).
- 106. N. N. da Silva, I. M. Abreu, J. R. Cerqueira, D. N. do Amaral, K. S. Garcia, L. T. S. Santos, O. M. C. Oliveira, A. F. de S. Queiroz, M. E. Machado, Paleoenvironmental characterization of the Ponta Grossa formation (Devonian) at the northwest border of the Paraná Basin, Brazil. J. South Am. Earth Sci. 130, 104540 (2023).
- I. Bobrovskiy, J. M. Hope, A. Krasnova, A. Ivantsov, J. J. Brocks, Molecular fossils from organically preserved Ediacara biota reveal cyanobacterial origin for *Beltanelliformis*. *Nat. Ecol. Evol.* 2, 437–440 (2018).
- 108. M. A. Ikeda, H. Nakamura, K. Sawada, Organic Geochemistry Aliphatic hydrocarbons in the lichen class Lecanoromycetes and their potential use as chemotaxonomic indicators and biomarkers. Org. Geochem. 179, 104588 (2023).
- G. D. Love, C. E. Snape, A. D. Carr, R. C. Houghton, Release of covalently-bound alkane biomarkers in high yields from kerogen via catalytic hydropyrolysis. *Org. Geochem.* 23, 981–986 (1995)
- G. Vinnichenko, A. J. M. Jarrett, J. M. Hope, J. J. Brocks, Discovery of the oldest known biomarkers provides evidence for phototrophic bacteria in the 1.73 Ga Wollogorang Formation, Australia. *Geobiology* 18, 544–559 (2020).

SCIENCE ADVANCES | RESEARCH ARTICLE

- 111. V. M. Dembitsky, Lipids of lichens. Prog. Lipid Res. 31, 373–397 (1992).
- 112. I. Bobrovskiy, A. Nagovitsyn, J. M. Hope, E. Luzhnaya, J. J. Brocks, Guts, gut contents, and feeding strategies of Ediacaran animals. *Curr. Biol.* **32**, 5382–5389.e3 (2022).
- 113. J. Brocks, I. Bobrovskiy, Some animals make plant sterols. Science 380, 455–456 (2023).
- I. Melendez, K. Grice, L. Schwark, Exceptional preservation of palaeozoic steroids in a diagenetic continuum. Sci. Rep. 3, 2768 (2013).
- B. A. Stankiewicz, D. E. G. Briggs, R. Michels, M. E. Collinson, M. B. Flannery, R. P. Evershed, Alternative origin of aliphatic polymer in kerogen. *Geology* 28, 559–562 (2000).
- K. J. Niklas, Chemical examinations of some non-vascular Paleozoic plants. *Brittonia* 28, 113–137 (1976)
- K. J. Niklas, W. G. Chaloner, Chemotaxonomy of some problematic palaeozoic plants. Rev. Palaeobot. Palynol. 22, 81–104 (1976).
- V. C. Farmer, The Infrared Spectra of Minerals (Mineralogical Society of Great Britain and Ireland. 1974): https://pubs.geoscienceworld.org/books/book/1871/.
- J. D. Russell, A. R. Fraser, "Infrared methods," in Clay Mineralogy: Spectroscopic and Chemical Determinative Methods, M. J. Wilson, Ed. (Springer, 1994), pp. 11–67; http://link. springer.com/10.1007/978-94-011-0727-3_2.
- W. M. K. Matsumura, N. M. Balzaretti, R. lannuzzi, Fourier transform infrared characterization of the Middle Devonian non-vascular plant *Spongiophyton*. *Palaeontology* 59, 365–386 (2016).
- H. Ganz, W. Kalkreuth, Application of infrared spectroscopy to the classification of kerogen types and the evaluation of source rock and oil shale potentials. *Fuel* 66, 708–711 (1987).
- D. Zdebska, On Spongiophyton from the Lower Devonian of Poland. Acta Palaeobot. 19, 13–20 (1978).
- 123. G. Pacyna, M. Barbacka, Polish Palaeobotany: 750 Million years of plant history as revealed in a century of studies. Palaeozoic macrofossils. *Acta Soc. Bot. Pol.* **91**, 9123 (2022).
- D. Edwards, Fragmentary non-vascular plant microfossils from the late Silurian of Wales. Bot. J. Linn. Soc. 84, 223–256 (1982).
- Y. Guo, D. Wang, Studies on plant cuticles from the Lower-Middle Devonian of China. Rev. Palaeobot. Palynol. 227, 42–51 (2016).
- E. M. Boureau, D. P. Pons, Sur des empreintes végétales dévoniennes du Sud de la Bolivie. Comptes Rendus l'Académie des Sci. 276, 2151–2153 (1973).
- A. D. Farjat, M. S. Riglos, J. L. Ortiz, Silurian and devonian heteroconchia cardiomorphi bivalves from Bolivia. Ameahiniana 58, 385–400 (2021).
- 128. M. Di Pasquo, S. Noetinger, P. Isaacson, G. Grader, D. Starck, E. Morel, H. A. Folnagy, Mid-Late Devonian assemblages of herbaceous lycophytes from northern Argentina and Bolivia: Age assessment with palynomorphs and invertebrates and paleobiogeographic importance. J. South Am. Earth Sci. 63, 70–83 (2015).
- P. Gerrienne, M. Fairon-Demaret, J. Galtier, H. Lardeux, B. Meyer-Berthaud, S. Régnault, Plants associated with tentaculites in a New Early Devonian locality from Morocco. *Abh. Geol. Bundesanst.* 54, 323–335 (1999).
- W. M. K. Matsumura, R. lannuzzi, Plantas devonianas do Brasil e seu significado bioestratigráfico. Bol. Mus. Para. Emílio Goeldi, Ciênc. Nat. 10, 19–36 (2021).

- M. Radke, Application of aromatic compounds as maturity indicators in source rocks and crude oils. Mar. Pet. Geol. 5, 224–236 (1988).
- K. E. Peters, C. C. Walters, J. M. Moldowan, The Biomarker Guide (Cambridge Univ. Press, 2004); www.cambridge.org/core/product/identifier/9781107326040/type/book.

Acknowledgments: We acknowledge the facilities for the nanoCT (MOGNO beamline, Sirius: proposal 20221825), nanoXRF (CARNAUBA beamline, Sirius; proposal 20220340), microFTIR (IMBUIA beamline, Sirius: proposal 2022044; and IPANEMA lab, Soleil: IPERION proposal fix_182), XANES (IPE beamline, Sirius: proposal 20221000), ptychography (CATERETE beamline, Sirius: 20222075), SR-XRD/PDF and XRD-CT (1-ID beamline, APS: proposal 80784), microCT (DIAD, DLS: MG-32319), and XPS (LNNano: proposal 20230172) measurements. This research also used resources of the Advanced Photon Source (contract no. DE-AC02-06CH11357). We are grateful for the support given by S. B. Betim and N. C. Moreno at the Chemistry Laboratory (LNLS) and J. Hope (ANU). We further acknowledge the Institute of Geosciences (University of São Paulo), Centro Regional para o Desenvolvimento Tecnológico e Inovação (CRTI, UFG), T. C. R. Rocha (LNLS), C. A. S. de Medeiro (LAM, LNLS), R. D. Ribeiro (UMA, CNPEM), D. Y. Kakizaki (UMA, CNPEM), and J. S. Alencar (LNNano, CNPEM). R.O.F. acknowledges the support from CNPq (309946/2021-2). A.C. was supported by the NSF-EAR award 2051199. Funding: B.B.-K. was supported by FAPESP (grants 2020/11320-0 and 2022/06133-1). J.O.-H. and B.B.-K. are supported by the Lemann Foundation. Author contributions: B.B.-K. designed the project. B.B.-K., N.L.A., V.P., and C.B.R. conceived and designed the XRD, XRD-CT, PDF, and nanoCT experiments. J.J.B. performed and interpreted the pyrolysis-GC-MS and GC-MS experiments. E.R.A., R.G., T.P., and B.B.-K. designed and performed the ¹³C SS-NMR experiments and interpreted the results. A.A. performed the XPS measurements, and B.B.-K. interpreted the results. M.A.K. and B.J. performed the nitrogen isotopes analysis. O.H.A. performed the organic petrography investigation and Rock-Eval pyrolysis. D.P. and J.C. designed and performed the LA-ICPMS. B.B.-K., A.C., R.O.F., and M.T. designed and performed the multispectral imaging and microFTIR investigations, H.L.S.M.P., C.M.A.O., B.B.-K., and G.M.E.M.P. performed the ToF-SIMS experiments. B.B.-K., F.C.V., and L.G.F.B. designed and conducted the N K-edge XANES. B.B.-K., N.L.A., C.B.R., J.A., and J.-S.P. designed and performed the SR-XRD and PDF measurements, and J.A. and J.-S.P. processed the 3D datasets. B.B.-K., N.L.A., and S.A. designed and performed the nanoCT measurements at Diamond Light Source. C.C.P. performed and processed the ptychography datasets. J.O.-H. and R.L.-A. contributed to the interpretation of results and writing. B.B.-K., L.d.M., M.F., G.M.E.M.P., and M.A.S.B. conducted the field work. B.B.-K. wrote the manuscript with significant input from all authors, B.B.-K., R.G., M.T., S.A., L.G.F.B. Â.A., D.P., L.d.M., C.B.R., O.H.A., and M.A.K. contributed to data curation. Competing interests: The authors declare that they have no competing interests. Data and materials availability: All data needed to evaluate the conclusions in the paper are present in the paper and/or the Supplementary Materials.

Submitted 15 February 2025 Accepted 1 October 2025 Published 29 October 2025 10.1126/sciadv.adw7879